Charles University

Faculty of Science

Department of Applied Geoinformatics and Cartography

Study programme: Geography

Branch of study: Cartography and geographic information systems

Bc. Daniel Paluba

A correction of the local incidence angle of SAR data: a land cover specific approach for time series analysis

Korekce lokálního dopadového úhlu SAR dat pro analýzu časových řad: metoda specifická pro krajinný pokryv

Diploma thesis

Supervisor: doc. RNDr. Přemysl Štych, Ph.D.

Prague, 2020

Vysoká škola: Univerzita Karlova **Fakulta:** Přírodovědecká

Katedra: Aplikované geoinformatiky a kartografie **Školní rok:** 2019/2020

Zadání diplomové práce

pro Bc. Daniel Paluba

obor Kartografie a geoinformatika

Název tématu: A correction of the local incidence angle of SAR data: a land cover specific approach for time series analysis

Zásady pro vypracování

V současnosti se čím více využívají radarová satelitní (SAR) data na monitorování stavu a dynamiky krajinné pokrývky. Průnik radarového signálu přes mlhu a oblaka, snímaní ve dne i v noci představují mnohdy obrovskou výhodu oproti často využívaným optickým datům. Nároky na výpočetní techniku jsou na jejich zpracování vyšší, hlavně při zpracování dlouhých časových řad. K zajištění co nejvyššího možného časového rozlišení dat SAR je nutné použít všechny dostupné dráhy družic nad daným územím. To může představovat výzvu v hornatém terénu, kde boční snímání družic SAR v kombinaci s různými sklony a aspekty terénu může silně ovlivnit intenzitu radarového zpětného rozptylu. Tuto závislost způsobenou terénem je třeba odstranit. Ačkoli v literatuře jsou popsány metody, které se zabývají tímto problémem, žádná z těchto metod není připravena pro operativní a snadno přístupnou analýzu časových řad v horských oblastech.

Hlavním cílem této práce bude vytvořit algoritmus na eliminaci vlivu terénu pro lesní ekosystémy k účelům analýz časových řad. Ideálním nástrojem pro vývoj této metody může být cloudová platforma Google Earth Engine, kde je potřeba implementace podobné metody pro radarové data. Metodu je potřeba řádně otestovat, případně porovnat s tradičně využívanou metodou pro korekce vlivu terénu, tzv. Terrain Flattening.

Konkrétními výsledky budou:

- rešerše relevantní odborné literatury v monitorování lesa pomocí radarových dat
- návrh algoritmu na eliminaci vlivu terénu
- výsledky testování navržené metody
- volně přístupná funkce/modul do Google Earth Engine

Rozsah grafických prací: podle potřeby

Rozsah průvodní zprávy: cca 40 – 80 stran

Seznam odborné literatury:

BAYER, T., WINTER, R., SCHREIER, G. (1991): Terrain influences in SAR backscatter and attempts to their correction. IEEE Transactions on Geoscience and Remote Sensing, 3, 29, 451–462.
CASTEL, T., BEAUDOIN, A., STACH, N., STUSSI, N., LE TOAN, T., DURAND, P. (2001): Sensitivity of space-borne SAR data to forest parameters over sloping terrain. Theory and experiment. International Journal of Remote Sensing, 12, 22, 2351–2376.
DOSTÁLOVÁ, A., WAGNER, W., MILENKOVIĆ, M., HOLLAUS, M. (2018): Annual seasonality in Sentinel-1 signal for forest mapping and forest type classification. International Journal of Remote Sensing, 21, 39, 7738–7760.
FLORES-ANDERSON, A. I., HERNDON, K. E., THAPA, R. B., CHERRINGTON, E. (2019): The SAR Handbook: Comprehensive Methodologies for Forest Monitoring and Biomass Estimation. SERVIR Global Science Coordination Ofce National Space Science and Technology Center, Huntsville, AL, United States.
GORELICK, N., HANCHER, M., DIXON, M., ILYUSHCHENKO, S., THAU, D., MOORE, R. (2017): Google Earth Engine: Planetary-scale geospatial analysis for everyone. Remote Sensing of Environment, 202, 18–27.
HINSE, M., GWYN, Q. H. J., BONN, F. (1988): Radiometric Correction of C-Band Imagery for Topographic Effects in Regions of Moderate Relief. 2, 26, 122–132.
RAUSTE, Y. (1990): Incidence-angle dependence in forested and non-forested areas in Seasat SAR data. International Journal of Remote Sensing, 7, 11, 1267–1276.
SMALL, D. (2011): Flattening gamma: Radiometric terrain correction for SAR imagery. IEEE Transactions on Geoscience and Remote Sensing, 8, 49, 3081–3093.

Vedoucí bakalářské práce:	doc. RNDr. Přemysl Štych, Ph.D.
Datum zadání bakalářské práce:	14. 01 .2019
Termín odevzdání bakalářské práce:	14. 09. 2020

Platnost tohoto zadání je po dobu jednoho akademického roku.

…… .....……

Vedoucí bakalářské práce Vedoucí katedry

V Praze dne

Prohlášení

Prohlašuji, že jsem závěrečnou práci zpracoval samostatně a že jsem uvedl všechny použité informační zdroje a literaturu. Tato práce ani její podstatná část nebyla předložena k získání jiného nebo stejného akademického titulu.

V Praze, 13.09.2020 .....

Bc. Daniel Paluba

Acknowledgement:

Firstly, I would like to express my sincere gratitude to my supervisor doc. RNDr. Přemysl Štych, Ph.D., for support of my diploma thesis, for his valuable advices, comments, and time devoted to the elaboration of this diploma thesis. I would also like to thank Google for free access to Google Earth Engine. Special thanks go to my girlfriend, Zsóka, for her patience with me during the preparation of this work and for her unceasing encouragement and enthusiastic support. Last but not the least, I would like to thank my family and friends for their motivation and support during my whole studies.

Abstract

To ensure the highest possible temporal resolution of SAR data, it is necessary to use all the available acquisition orbits and paths of a selected area. This can be a challenge in a mountainous terrain, where the side-looking geometry of space-borne SAR satellites in combination with different slope and aspect angles of terrain can strongly affect the backscatter intensity. These errors/noises caused by terrain need to be eliminated. Although there have been methods described in the literature that address this problem, none of these methods is prepared for operable and easily accessible time series analysis in the mountainous areas.

This study deals with a land cover-specific local incidence angle (LIA) correction method for time-series analysis of forests in mountainous areas. The methodology is based on the use of a linear relationship between backscatter and LIA, which is calculated for each image separately. Using the combination of CORINE and Hansen Global Forest databases, a wide range of different LIAs for a specific forest type can be generated for each individual image. The algorithm is prepared and tested in cloud-based platform Google Earth Engine (GEE) using Sentinel-1 open access data, SRTM digital elevation model, and CORINE and Hansen Global Forest databases.

The method was tested in 15 study areas in the Central Europe. The results achieved by our method showed a reduction of statistical parameters (variance, standard deviation, and range of backscatter values) of forest points in these areas. The most significant reduction (by more than 50 %) was achieved in areas with a wide range of LIAs, while in areas with a low LIA ranges the effect of correction was very low. In comparison with the behaviour of time series before and after correction, four case studies with different LIA ranges were further tested. Time series after the correction showed a reduced fluctuation of backscatter values (caused by different LIAs in each acquisition path), while this reduction was more significant in areas with a large difference in LIAs. The proposed method was also compared to a widely used desktop-based method of Terrain Flattening. The proposed method showed a greater reduction of fluctuations in time series caused by different acquisition pathways, while the computational time of these methods is incomparable. Our method was implemented in GEE as a freely available function, making the method available to a wide remote sensing community.

Key words: local incidence angle, correction, time series, google earth engine, forest monitoring

Abstrakt

K zajištění co nejvyššího možného časového rozlišení dat SAR je nutné použít všechny dostupné dráhy družic nad daným územím. To může představovat výzvu v hornatém terénu, kde boční snímání družic SAR v kombinaci s různými sklony a aspekty terénu může silně ovlivnit intenzitu zpětného radarového rozptylu. Tyto chyby způsobené terénem je třeba odstranit pro možné porovnání dat v čase. Ačkoli v literatuře jsou popsány metody, které se zabývají tímto problémem, žádná z těchto metod není připravena na operativní a snadno přístupnou analýzu časových řad v horských oblastech. Tato studie se zabývá metodou korekce lokálního dopadového úhlu (LIA) pro analýzu časových řad lesů v horských oblastech. Metodika je založena na použití lineární závislosti mezi radarovým zpětným rozptylem a LIA, který se počítá pro každý satelitní snímek zvlášť. Použitím kombinace databází CORINE a Hansen Global Forest můžeme pro každý jednotlivý snímek získat širokou škálu různých LIA pro konkrétní typ lesa. Algoritmus korekce byl připraven v cloudové platformě Google Earth Engine (GEE) s využitím volně dostupných dat Sentinel-1, digitálního modelu terénu SRTM a databází CORINE a Hansen Global Forest.

Metoda byla testována na 15 případových studiích ve střední Evropě. Výsledky dosažené naší metodou ukázaly snížení nežádoucích hodnot statistických ukazatelů (rozptylu, směrodatné odchylky a rozpětí hodnot radarového zpětného rozptylu) pro vybrané oblasti zájmu v lesních ekosystémech Česka. Nejvýraznější snížení (o více než 50 %) bylo dosaženo v oblastech s širokým rozsahem různých LIA, zatímco v oblastech s nízkým rozsahem LIA byl účinek korekce velmi nízký (nižší než 10%). Při srovnání s chováním časových řad před a po korekci byly dále testovány čtyři případové studie s různými rozsahy LIA. Časové řady po korekci ukázaly snížené kolísání hodnot zpětného rozptylu (způsobené různými LIA v každé akviziční dráze). Navržená metoda byla také porovnána s nejčastěji používanou metodou, tzv. Terrain Flattening, v desktopovém prostředí. Navržená metoda pak ukázala větší snížení fluktuace časové řady způsobených různými akvizičními dráhami, zatímco výpočetní čas těchto metod byl neporovnatelný. Naše metoda byla implementována v GEE jako volně dostupná funkce, co umožní přístup k této funkci široké komunitě zabývající se zpracováním SAR oblasti dálkového průzkumu Země.

Klíčová slova: lokální dopadový úhel, korekce, časové řady, Google Earth Engine, monitorování lesů

TABLE OF CONTENTS

List of figures and tables

Figures

Tables

List of symbols and abbreviations used

List of symbols used

a	offset of the linear regression
b	slope of the linear regression
h	average difference in elevation
i	look vector
n	vector vertical to the surface
q	slope of the linear regression between σ_θ^0 and $\cos(\theta_0)$
α	terrain slope
β	terrain aspect
γ	viewing azimuth of the sensor
ε_r	dielectric constant
θ	radar incidence angle
θ_0	local incidence angle
θ_{ref}	reference incidence angle
λ	wavelength
σ^0	backscattering coefficient
σ_0^0	backscatter value at his original local incidence angle θ_0
σ_θ^0	normalized (corrected) radar backscatter
σ_{ref}^0	calculated backscatter value for the given reference incidence angle (corrected backscatter)

List of abbreviations used (in alphabetical order)

API	application programming interface
ASAR	Advanced Synthetic Aperture Radar
CAPI	computer-assisted image interpretation
CLC	CORINE Land Cover
dB	decibel
DEM	Digital Elevation Model
EEA	European Environment Agency
ESA	European Space Agency
ETM+	Enhanced Thematic Mapper Plus
EU	European Union
EW	Extra-Wide swath
GEE	Google Earth Engine
GRD	Ground Range Detected
IDE	interactive development environment
InSAR	interferometric SAR

IQR	interquartile range
IW	Interferometric Wide swath
LAI	leaf area index
LIA	local incidence angle
MAAP	Multi-Mission Algorithm and Analysis Platform
MMU	minimum mapping unit
MMW	minimum width of linear element
NASA	National Aeronautics and Space Administration
NDMI	Normalized Difference Moisture Index
NDVI	Normalized Difference Vegetation Index
NESZ	Noise Equal to Sigma Zero
NP	national park
OLI	Operational Land Imager
PLA	protected landscape area
RMSE	Root Mean Square Error
RS	Remote Sensing
RVI	Radar Vegetation Index
SAR	synthetic aperture radar
SCL	Single Look Complex
SM	Strip Map
SRTM	Shuttle Radar Topography Mission
TF	terrain flattening
VHF	Very High Frequency
WM	Wave mode

Introduction

In remote sensing (RS), the 21st century is called to as the era of big data, when we have a huge amount (not only) of freely available data. When processing a larger amount of data, it is necessary to use tools that can process them effectively and quickly enough. In some cases, we may already encounter time and performance issues and limitations on a traditional desktop software. It is necessary to download, pre-process data and then we can perform analyses on them. In recent years, in RS and in the use of big data, so-called cloud platforms have become widely used. They store not only images and data archives, but they also bring the computing technology needed for data processing.

In forest monitoring, multispectral optical satellite data, have been proven to be a very effective data source. In many cases, however, optical data have certain shortcomings, especially regarding clouds. In the microwave electromagnetic spectrum of radar sensors, the signal can penetrate clouds and fog and is not dependent on the light of the Sun, so sensors can scan during the day and at night. Additionally, they can be potentially used in monitoring landscape changes as complementary to optical data (i.e. in Ranson et al. 2003). Since the launch of Sentinel-1 in 2014 with freely available data, interest in synthetic aperture radar (SAR) data has begun to grow and new methods has begun to be developed. Systematic sensing of the earth's surface with constant geometric characteristics of the sensors brought many advantages over previous radar missions.

However, the SAR signal is interacting with the surface in a totally different way as in optical data. One of the main differences are caused by the side-looking geometry of SAR data - areas from the same land cover class can have different backscatter, indicating that they belong to a different class or show a change in the case of time series analysis, although no change has occurred. The most relevant problem can be experienced in data acquired over mountainous areas where orientation and slope of the terrain can influence the resulted backscatter. This factor is the most visible on the intensity of the received signal when combining images from different orbits and paths of the satellite (ascending vs. descending, or adjacent paths covering a given area). This is especially important over forests, because most of the forests of Central Europe are located in mountainous areas. In time series analysis, this effect can be seen as a constant fluctuation of the reflectance values acquired from different successive paths.

To obtain an accurate information that represents a real status or change in the area, it is necessary to eliminate the aspect of terrain.

There are several techniques to correct the topographic effects. Currently the most used algorithm for correction of topographic effect is the so-called Radiometric Terrain Flattening developed by Small (2011). This method is available in desktop software such as SNAP Sentinel-1 Toolbox. However, in the case of the cloud platforms (e.g. Google Earth Engine – GEE), neither this method nor other methods to eliminate the effects of the terrain are available.

The presented study deals with an innovative method of land cover-specific correction of the local incidence angle (LIA) using a linear regression analysis in the mountainous areas for time-series analysis in GEE. The main difference between currently used regression-based normalisation approaches and the presented method is on the use of single image to calculate the dependence of backscatter values of selected forest type on LIA. This is allowed by using available land cover databases including data representing only the specified land cover class, so for each Sentinel-1 image we can calculate the backscatter-LIA dependence separately. Next method aspect is the use of site- and path-specific reference incidence angle. Using this algorithm, the terrain effects in the time series curve are eliminated.

The main aim of the study is to prove, that the developed method is suitable for eliminating the effect of the terrain. The accuracy and suitability of the proposed method is tested by statistical evaluation of forest areas backscatter after the correction on forests with different characteristics - at different elevation, terrain slope and orientation, with different LIAs. Also, the effectivity of the method is tested on short-term time series analyses of coniferous and deciduous forests. The proposed method is compared to the most used method for eliminating terrain effects - to the Radiometric Terrain Flattening.

The first chapter of this work examines the various effects that influence radar backscatter, focused mainly on forest areas. The second chapter describes the study areas, data, platform, and software used in this study, as well as the methodology of this work. The third chapter describes the results and the fourth chapter is aimed on a discussion of the achieved results. The fifth chapter contains conclusions and future plans in working with the developed method.

1 Literature review and introduction to the topic

1.1 Radar data – specification

Radar satellite systems operate in the microwave region of the electromagnetic spectrum with a wavelength from 1 mm to 1 m and a frequency of 0.3 to 300 GHz. This broad spectrum is divided into several bands, while the most common bands used in spaceborne radar remote sensing are L-, C- and X-bands. In tab. 1 different radar bands are listed with their characteristics and typical applications. Compared to optical data which are sensitive to the surface of objects, radar data provide information on the geometric and dielectric properties of the object.

Tab. 1 Characteristics of individual bands of microwave radiation

Band	Frequency (GzH)	Wavelength (cm)	Typical application
P-band	0.3 - 1.0	100 - 30	Biomass. First P-band spaceborne SAR will be launched ~2020; vegetation mapping and assessment. Experimental SAR.
L-band	1 - 2	30 - 15	Medium resolution SAR (Geophysical monitoring; biomass and vegetation mapping; high penetration; InSAR)
S-band	2 - 4	15 - 7.5	Little but increasing use for SAR-based Earth observation; agriculture monitoring (NISAR will carry an S-band channel; expands C-band applications to higher vegetation density)
C-band	4 - 8	7.5 - 3.8	SAR workhorse (global mapping; change detection; monitoring of areas with low to moderate vegetation; improved penetration; higher coherence); Ice, ocean, maritime navigation
X-band	8 - 12	3.8 - 2.4	High-resolution SAR (urban monitoring; ice and snow, little penetration into vegetation cover; fast coherence decay in vegetated areas)
Ku-band	12 - 18	2.4 - 1.7	Rarely used for SAR (satellite altimetry)
K-band	18 - 27	1.7 - 1.1	Rarely used (H2O absorption)
Ka-band	27 - 40	1.1 - 0.8	Rarely used for SAR (airport surveillance)

Source: adopted from Flores-Anderson et al. (2019), p. 29

As radar sensors can measure at much higher wavelengths than sensors of optical satellites, they can detect completely different surface properties (Richards 2009). Backscattering coefficient (σ^0) gives us information about the scanned surface/object. It is expressed in decibels (dB) and is given as the ratio of the energy received by the sensor to what it would receive if the surface scatters the incident energy in an isotropic manner (Patnaik 2017). Similarly as in case of optical data, different land cover classes have different backscatter responses in radar data. Mougin et al. (1995), in their global backscattering analysis, observed the lowest values of backscatter over deserts (up to -24 dB), where huge spatial variations (up to 18 dB) were observed due to local topography. The highest values were present over snow- and ice-covered regions (> -5

dB). The highest backscatter among vegetated areas was measured over tropical forests (around -7 dB). They suggested that seasonal variations should help to distinguish different land cover classes and found seasonal variations in backscatter values over areas which pronounce a known seasonal vegetation activity. On the other hand, comparison of backscatter over tropical evergreen forest and deserts from different seasons showed only a little, insignificant variation. These results are however, influenced by several other factors.

1.2 Effects influencing radar backscatter over forests

The interaction between the SAR backscatter (σ^0) and the surface depends primarily on the characteristics of the studied object - on the surface roughness and dielectric properties of the object (Freeman 1992), and on the sensor characteristics, i.e. on wavelength (frequency), angle of incidence and polarization (Paloscia, Santi, Pettinato 2015; Rüetschi, Small, Waser 2019; Yunjin Kim, van Zyl 2002; Patnaik 2017). For forest areas, where usually a volume scattering is occurring, the dominant factor is "the composition of the medium, in terms of particle size and orientation" (Freeman, 1992, p. 1109). Characteristics of the studied object are different for each land cover class and can be biased by some environmental factors, like change in vegetation activity, moisture, temperature, etc. The sensor characteristics are fixed for each sensor and they will be the same over all kind of land cover classes. While the wavelength and polarization are constant throughout the image, the angle of incidence (we will refer to that as radar incidence angle in the next parts of the thesis) is increasing from the near to the far range of the image. This causes variations of the backscatter values for a given land cover class – different backscatter for the same class at different radar incidence angles. This difference must be corrected. However, the correction of radar incidence angle can be valid only for ideal situations, where the effect of terrain should be neglected, e.g. over relatively flat terrain or over sea. On the other hand, in case of areas with tilted terrain, the incidence angle of the electromagnetic wave is affected by the slope and aspect of the studied terrain. Thus, effect of the terrain needs to be considered and eliminated for appropriate evaluation and interpretation of obtained backscatter. This is especially important over forests, because most of the forests of Central Europe are located in mountainous areas.

The next part of this work focuses on the description of individual characteristics of the sensor and the object that may affect the backscatter of forests. The last part focuses on the main interest of this work, on possible ways to eliminate the terrain effects.

1.3 Sensor characteristics influencing radar backscatter over forests

1.3.1 Dependence on the wavelength

In general, at longer wavelengths, the penetration of the signal through the vegetation canopy or below the surface is greater. Comparison of P-, L- and C-bands by Paloscia (1998) showed different influence of vegetation biomass and crop morphology on the backscatter at each band, e.g. herbaceous vegetation, seemed transparent at the P-band, and different agricultural crops such as sunflower and corn could be identified at the L-band (due to larger stems and leaves). A clear positive linear dependence of biomass and backscatter at P-, L- and C-band was found also in Dobson et al. (1992), while this dependence is found to be decreasing with frequency as the contribution of the upper layer of the canopy to the backscatter becomes more significant. Thus, in case of high frequency (short wavelength), such as C-band, microwave energy is reflected mainly from the top layer of the tree crown and less from the bottom of the crown, while at lower frequencies (e.g. in L-band) the signal has higher penetration and is reflected also from under the crown (Rüetschi, Small, Waser 2019) (see fig. 1). Similarly, several earlier studies also proved that the backscatter over forests at C-band is mainly originating in volume scattering that takes place in the canopy layer of trees (Chauhan, Lang, Ranson 1991; Durden, Klein, Zebker 1991; Wu 1985; Luckman 1998; Dobson et al. 1992). Paloscia et al. (2015) stated that the C-band signal is sensitive to the presence or absence of leaves. As reported by Chauhan et al. (1991) needles and branches of coniferous forests cause large attenuation (about half of the total attenuation caused by forest canopy) and prevent the deeper penetration of a C-band wave into the canopy, therefore having the biggest contribution to the total backscatter. According to their results, the backscatter from the trunk is very little at the C-band and it will not reach the ground layer through trees higher than 15 meters. They also stated that needles and branches act as Rayleigh scatterers and their attenuation increases with frequency, while at X-band the contribution from needles become the most dominant. Finding, that the signal at C-band penetrates vegetation only partially and interacts only with leaves or needles and small branches was proved also in a more recent study by Reiche et al.

(2018), who added that backscatter from leaves and branches is largely sensitive to roughness and humidity of the canopy.

In the available literature, L-band is the most used band for forest research (e.g. Mitchell et al., 2017) and the longer wavelength L-band is suitable for the study of deforestation, while the shorter wavelength C-band is less useful for that, because of low penetration and greater signal saturation over forests (Woodhouse (2005) cited in Reiche et al. (2018)). Despite of these findings, according to the literature review above about the sensitivity of backscatter at shorter wavelength to forest canopy, C-band data seems to be sufficient for monitoring forests and their changes over time. The next section will focus on findings on forest backscatter response mainly at C-band and on its comparison with other bands.

Fig. 1 Reflectivity of black pine at different wavelengths.

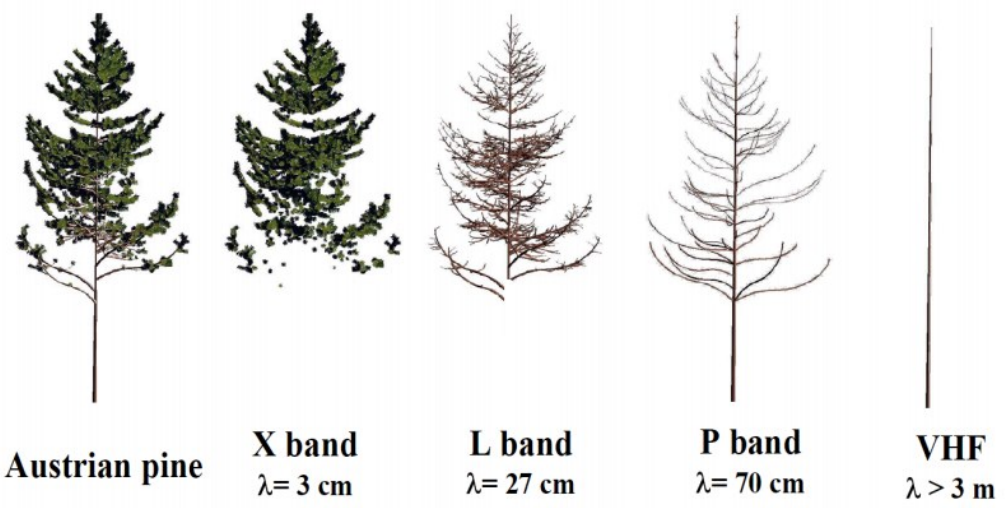

Source: Le Toan (2007), p. 66. *Explanatory Notes: VHF - Very High Frequency*

1.3.2 Effect of polarization

Polarization represents the orientation of the electric and magnetic component of an electromagnetic wave that are perpendicular to each other and to the direction of movement of the electromagnetic wave (Richards 2009). Radar antennas transmit a signal either vertically (V) or horizontally polarized (H) and the same happens when a signal is received – it is received either horizontally or vertically, creating 4 different situations: when transmitted in H and received in H polarization, so it is the so called

HH polarization. Other ones are VV, HV or VH. The use of different polarizations increases the information value of the data and can be used, for example, to recognize different types of surfaces. This section presents findings on the effect of polarization in distinguishing different types and characteristics of forests.

Different polarizations were investigated in Bousbih et al. (2017) in obtaining Leaf Area Index (LAI) and height of agricultural crops from Sentinel-1 images. They found that as LAI increases, vegetation more attenuates the backscatter from the soil towards the sensor. That behaviour was stronger in VV polarization, compared to VH, where vegetation parameters had almost no effect on the resulted backscatter. Authors attributed low sensitivity of vegetation parameters in VH polarization to volume scattering effects, in which there are huge amount of scattering due to randomly oriented elements such as canopy components (Richards 2009).

Combining different polarizations helps to improve the separability of forest types. It has been proven in the work of Wu (1985), where the backscatter response over deciduous, coniferous, and mixed forests at C-band of an airborne scatterometer was analysed. He figured out that the backscatter over deciduous forests is the highest among others and found some differences in polarizations: a) generally for each forest type, the VH polarization backscatter value is the lowest compared to VV and HH, b) the highest backscatter for mixed forest was in VV polarization, while for coniferous forest it was in HH, c) deciduous forests with no significant understory had the same polarization characteristics as coniferous forests and d) coniferous forest with some understory had the same polarization characteristics as mixed forests. Furthermore, he observed a deeper penetration of HH polarization to the base of the forest canopy for high incidence angles, while signal in VV polarization was able to penetrate only a few meters to the canopy. Another finding was that, generally the backscatter from trees is increasing with the increase of signal's attenuation in the canopy. Chauhan et al. (1991) also showed that horizontal waves penetrate more deeply to the canopy than vertical waves.

Discrimination between deciduous and coniferous forests was also proven for VV polarization of C-band data in Proisy et al. (2000), where the difference between them was about 1 dB. Authors attributed this difference to the influence of non-forest parameters, like understory vegetation. However, the separability between different deciduous forest types and species has not been proved.

For distinguishing between coniferous stands with different forest biomass (sparse and dense forest) the C-band HH and VV polarizations have been found to be suitable in Durden et al. (1991).

In the case of sensitivity to changes in forest, Reiche et al. (2018) pointed out that the single polarized (VV) signal of the C-band Sentinel-1 image was less sensitive compared to cross-polarized (VH). Tanase et al., (2018) showed that wind and insect disturbances cause changes in the backscatter values and the highest sensitivity was observed in the cross-polarized channel (HV) of the L-band ALOS PALSAR images.

Polarimetric parameters

To investigate types of vegetation and their changes, the so-called polarimetric parameters have been developed. Polarimetric parameters are divided into absolute and relative (based on Kim & van Zyl (2002)). The category of absolute parameters includes the cross-sections (i.e., HV and VH) and eigenvalues. Relative parameters include the HH and VV correlation coefficients, entropy, anisotropy and the Radar Vegetation Index (RVI) developed by Kim & van Zyl (2000). Kim & van Zyl (2002) found that relative polarimetric parameters are more rapidly saturated than absolute parameters, while backscatter from cross-sections (HV and VH) is saturated with increasing biomass. They added, that polarimetric parameters are the most suitable for monitoring the degree of regeneration of vegetation, especially when time series are available.

Earlier studies have also used, for example, the so-called cross-polarization ratio (HV / HH and HV / VV) (e.g. Dobson et al. (1992)), which seemed to be the best for estimating vegetation parameters.

Kim & van Zyl (2000) recommended that the most important step in developing parameters (indexes/indicators) is to find out what the polarimetric parameter is the most sensitive to in relation to the required geophysical information. The authors evaluated the sensitivity of the polarimetric parameter to the variation of physical properties and pointed out to the relationship between physical and polarimetric parameters.

1.3.3 Angle of incidence (radar incidence angle)

The radar incidence angle θ is the angle between the direction of incident radiation and the normal to the surface at the point of impact on the Earth's surface (Flores-

Anderson et al. 2019). The incidence angle is not stable across the image – it increases from near to far range of the image causing changes to the backscatter response. Images acquired from different orbits or paths will have different incidence angles over a given area resulting in various backscatter values, even if no changes have occurred in that area. Thus, in case of using the entire image for analysing the given land cover class or using a combination of several images from different paths and orbits to analyse the backscatter over a given area, variations resulted from the off-nadir viewing geometry of the radar sensor must be considered (Foody 1986). This is the case when using SAR images with wide range of incidence angles, usually spaceborne radar sensors, like the Advanced Synthetic Aperture Radar (ASAR) on the Envisat satellite which have incidence angles ranging from 15° to 45° (Torres et al., 2000), but also the Sentinel-1, ranging from 31° to 46° (Torres et al., 2012).

Gauthier et al. (1998) found a difference up to 2.7 dB in the ERS-1 C-band backscatter coefficients derived from the opposite orbits for the same agricultural fields. As a possible explanation for that they compared the influence of three following factors: 1) environmental factors, 2) SAR processor instability and 3) aspect and incidence angle sensitivity. They found that only the latter can be significantly attributed to the observed difference, even though the difference in incidence angle between opposite orbits was only up to 4° for the investigated areas.

Nguyen et al. (2015), in their study of mapping rice seasonality, noticed that the influence of radar incidence angle on backscatter is higher for bare soil than for densely vegetated areas. Because of the radar incidence angle influence on backscatter, they normalized (corrected) the data for different radar incidence angles (different look angles caused by different paths and orbits). In other studies, analysing of sea ice (Makynen, Karvonen 2017) and sea surface backscatter (Topouzelis, Singha 2016), there was also a need for eliminating the effects of different radar incidence angles.

On the other hand, Kaasalainen et al. (2010) decided to use images from the same imaging geometry, therefore to avoid the effects of topography on backscatter values. Similarly, in Rauste et al. (2016), Sentinel-1 images acquired in the same orbit configuration was used for mapping clear-cut sites.

1.4 Dependence on object characteristics influencing radar backscatter over forests

1.4.1 Dependence on geometrical characteristics of the studied object

According to Rayleigh's rule, a surface can be considered rough if:

$$h > \frac{\lambda}{8 * \cos\theta} \quad (1)$$

where θ is the angle of incidence and λ and h are the signal wavelength and the average difference in elevation of this surface, respectively. Conversely, a surface is considered smooth if:

$$h < \frac{\lambda}{8 * \cos\theta} \quad (2)$$

This implies that the surface roughness depends on the signal wavelength and the incidence angle (Richards 2009). These formulas show that at a constant angle of incidence, a surface with a given height difference (h) can be considered rough at short wavelengths, while smooth at long wavelengths.

In the case of forest ecosystems, we should consider the roughness of the crown surface and the entire canopy of a tree, where the roughness is contributed, for instance, by the size, shape and orientation of the tree crown components (leaves, fruits, etc.). That is why crops and trees with different structures and characteristics can be distinguished using their backscattering coefficient (Forkuor et al. 2014).

It was proven that the increase of vegetation density causes increase in backscatter (Sharma et al. 2005), while clear-cuts with greater density of recovery vegetation can cause difficulties in their separability from forests. Confusion in separability of clear-cuts and forests was noticed also in Ahern et al. (1993), where C-band CCRS SAR data in HH polarization with wavelength of 10 cm was used (which belongs more to the S-band). They found that the three investigated coniferous species were well separable in each season, while in summertime (August) it gave the best results. On the other hand, separability of deciduous species was low. This can be explained by the use of only one image per season (four seasons). They observed higher backscatter from deciduous trees without leaves than with leaves, which interpreted as the effect of higher absorption or forward-scattering of backscatter by leaves. However, this is in contrast with earlier mentioned studies (Wu 1985), where the increase of backscatter with the increase of biomass was proven. This can be explained by the use of only one image per season in

the study by Ahern et al. (1993), where short-term variations in data could influence the results.

Rüetschi et al. (2019) found that C-band backscatter is suitable for rapid monitoring of major changes in forest structure, for example, changes after wind calamities. Based on their study, the increase of the reflected energy after a wind calamity may have 2 reasons: (1) increase in surface roughness due to fallen trees, (2) reduced attenuation of microwave energy in the tree canopy, resulting in increased reflectance from the surface. According to the findings of this study, the reflectivity of the area after wind calamity increases at lower wavelengths and decreases at higher wavelengths. Ranson & Sun (2000) proved that for land cover types with low vegetation, including clear cuts or small bushes, the ground surface contributes dominantly to the total backscatter.

Tanase et al., (2019) found that C-band had the highest sensitivity to LAI and foliage volume, and that the contribution of leaves to the backscatter was higher compared to the contribution of branches. According to these findings, as C-band data was mainly influenced by the foliage volume, they marked the ratio between co- and cross-polarized channels at C-band as appropriate for monitoring changes due to defoliation. In case of drought events, C-band can bring unsatisfactory results, however according to the assumption that in many cases drought events are accompanied with foliage loss, C-band can be used for monitoring these areas, too (Tanase et al. 2019). C-band signal sensitivity to defoliation was also observed in an earlier study using ERS-2 data in Kaasalainen et al. (2010), where a slight change was observed in the backscatter over the study areas with occurred defoliation, while for areas with no defoliation little or no change in backscatter was observed.

1.4.2 Dependence on dielectric properties of an object

"Dielectric properties of substances are expressed by their dielectric constant ε_r which value determines the reflectance of electromagnetic radiation at different wavelengths" (Kolář 2008). It measures the electrical properties of substances, each substance having a dielectric constant $\varepsilon_r \geq 1$, while the increasing of water content increases the reflectance and the value of the dielectric constant (e.g. dry soil has a dielectric constant 4, while water having approximately 81) (Richards 2009). Dielectric properties of the object can be biased by some environmental factors, like temperature or precipitation. The increased moisture content reduces the penetration of the radar

signal through vegetation or into the soil, thereby increasing their reflectivity (Walker 2016).

Wagner et al. (1999) claimed that the backscattering coefficient for vegetated areas is sensitive to the soil moisture content only in case of moderate or low vegetation, like grasslands or sparsely forested areas. Over agricultural areas, the sensitivity of C-band Sentinel-1 measurements to soil moisture changes was confirmed in the study by Bousbih et al. (2017). Furthermore, Szigarski et al. (2018) found that at longer wavelengths (such as in L-band), microwave indices are affected by soil moisture and surface roughness even in dense vegetation.

However, Frison et al. (2018) did not find out any relation between precipitation and backscatter values over forested areas using the C-band of Sentinel-1 mission. They explained this behaviour by the difference between the measured precipitation and the precipitation that can be retained by the leaves or needles of a tree. Tanase et al., (2019) also found that C-band was less sensitive to vegetation water content (variations about 1 dB) compared to P- and L-band.

On the other hand, Olesk et al. (2015) found a strong correlation between backscatter values and temperature using images acquired by C-band Sentinel-1 sensor. In addition, they found that a thick snow cover does not affect backscatter values – the backscatter value dropped 1 dB for images with a thin snow cover compared to snow-free image. Ranson & Sun (2000) found that freezing conditions generate low dielectric constants in boreal forests at L- and C-band data, which is reflected by the decrease of the backscatter value from tree canopy.

1.5 Effects of terrain and attempts to their correction

As mentioned before, effects of terrain can largely influence the backscatter over studied area, especially in case when combining images from different paths and orbits or analysing the backscatter response of a given land cover class across the entire image. For instance, Rauste (1990, p. 1267) found that “65 per cent of the total variation in land pixels can be attributed to terrain topography”. “The principal environmental factors that affect the radiometric quality of SAR images” include “combined effects of topography, slope, radar look angle and aspect” (Hinse, Gwyn, Bonn 1988, p. 122). With the calculation of local incidence angle (LIA), we can obtain a value which

involves all these factors. The accurate calculation of the local incidence angle is essential in avoiding errors in the further correction process (van Zyl et al. 1993).

Bayer et al. (1991) analysed the influence of different geometrical and imaging parameters as height, maximum slope, slope in the look direction, aspect of the maximum slope relative to the look direction at Seasat L-band and found that the local incidence angle had the strongest influence on the backscatter value. High dependence of backscatter on terrain topography was found in Rauste (1990) and he proved that with the increase of the incidence angle at L-band, different forest types become more separable and that the forest canopy is contributing significantly to the backscatter only at higher incidence angles. In an earlier study, Sun & Simonett (1988) found that at L-band HH polarized data, the dominant contribution to the backscatter is from the tree trunk for local incidence angles between 10° and 65°, whereas for large local incidence angles (65°-70°) the volume scattering from the canopy becomes dominant. In contrast to the studies at L-band, at C-band the volume scattering over coniferous forests was found to be the dominant scattering mechanism at the entire range of local incidence angles and that contribution of double-bounce scattering over coniferous forest was negligible at C-, L- and even at the P-band (Luckman 1998). Luckman (1998) also analysed the backscatter response over upland pastures using airborne SZAR data at P-, L- and C-band. He observed that at C-band data for low local incidence angles the volume scattering is a dominant scattering mechanism for pastures, while from about 30° of local incidence angle the surface scattering becomes dominant.

In addition, van Zyl (1993) noticed that the effect of topography on the forest floor, where scattering from ground and trunk layer may occur, is more prominent for longer wavelengths and HH polarization, like P-band, but this effect disappears at L-band (Van Zyl 1993). Durden et al. (1991) also confirmed, that in a relatively flat terrain the ground-trunk interaction is important only at P-band, compared to C- and L-band. However, they stated that for steep slopes the ground-trunk interaction might be smaller even at P-band caused by the change of their mutual geometries (angles between the trunk and the ground).

Castel et al. (2001) dealt with the effect of changing scattering caused by change in incidence angle for biomass retrieval from forested areas using JERS-1 and SIR-C L-band data. They suggested that in studies analysing forest stand parameters in hilly terrain it is important to also consider parameters as canopy height from which is possible to calculate the wave path length through the forest canopy in a sloping terrain.

However, in this method the knowledge or at least a close approximation of the real tree canopy height is expected. In contrast to them, Dostálová et al. (2016) proved, that at C-band, the forest height parameter has only very limited influence on backscatter response from forests, so it can be neglected.

There are several techniques to correct the topographic effects. Based on the reviewed literature, there are three main types of corrections which were used to correct the topographic effects. Among the very first approaches used to correct the topographic effect belong methods based on cosine correction (Topouzelis, Singha 2016; Hinse, Gwyn, Bonn 1988; Teillet et al. 1985; Bayer, Winter, Schreier 1991; Zhou, Zheng 2017). The second is based on statistical methods. Mladenova et al. (2013) identified two approaches within the group of statistical methods type which are based on: 1) linear or second order regression equations and 2) histogram/frequency matching. The third one is currently the most used type of correction, the so called Radiometric Terrain Flattening developed by Small (2011). Another classification of correction methods can be found in Bayer et al. (1991), where they grouped normalization models into three categories: a) cosine-based models, b) polynomial models, c) mean grey value models. They used 13 different empirical backscatter models for correction the relief effects in SAR images over vegetated areas.

1.5.1 Cosine square normalization

In the simplest way of normalization (correction) where the flat terrain and homogenous vegetation cover is assumed, the Lambert´s law for diffuse surfaces can be used (Teillet et al. 1985), which for the case of SAR backscatter is given by:

$$\sigma_\theta^0 = \sigma_0^0 \, cos^2(\theta) \tag{3}$$

where σ_θ^0 is the normalized (corrected) radar backscatter value of measured backscatter σ_0^0 and θ is the radar incidence angle. Clapp (1946) (cit. in Teillet et al. (1985)) found a better correlation to field data using the so-called Lommel-Seeliger model given by:

$$\sigma_\theta^0 = \sigma_0^0 \, cos(\theta) \tag{4}$$

In Topouzelis & Singha (2016), the cosine square normalization given by (3) was used for oceanographic application using ENVISAT ASAR WSM C-band data, where the effect of topography was not present. The equation given by (3) was adapted to create an equation, where the reference incidence angle (θ_{ref}) is assumed for the entire image (5):

$$\sigma^0_{ref} = \sigma^0_\theta \frac{cos^2(\theta_{ref})}{cos^2(\theta)} \tag{5}$$

where σ^0_{ref} represents the calculated backscatter value for the given reference incidence angle. In their study, the cosine square normalization produced worse results than the original image and the authors suggested that this type of normalization is not sufficient to use for wide swath SAR images.

In mountainous terrain it is much more important to remove the topographic effects. Zhou & Zheng (2017) used the same type of cosine square normalization given by (5) for radar glacier mapping and dry snow line mapping using Sentinel-1 images. They had to consider the elevation range in the study area, which was greater than 2500 meters, so instead of using the radar incidence angle θ they used local incidence angle θ_0:

$$\sigma^0_{ref} = \sigma^0_\theta \frac{cos^2(\theta_{ref})}{cos^2(\theta_0)} \tag{6}$$

In an earlier study by Hinse, Gwyn, Bonn (1988**)** also used equation (6), however the normalized backscatter value σ^0_θ was calculated differently, using the equation:

$$\sigma^0_\theta = b\, cos^q(\theta_0) + a \tag{7}$$

where b and a are coefficients representing slope and offset of the linear regression, respectively. The exponent q refers to the slope of the linear regression between σ^0_θ and $\cos(\theta_0)$. In addition, the square exponents of the cosine of reference and local incidence angles from (6) were calculated using semi-empirical functions to evaluate the relationship between the local incidence angle and the backscatter. The resulting equation was:

$$\sigma^0_{ref} = \sigma^0_\theta \frac{cos^q(\theta_{ref})}{cos^q(\theta_0)} \quad (8)$$

where, similarly as in (7), parameter *q* represents the slope of the linear regression. They assumed that the cosine of the local incidence angle *cos(θ)* represents the parameter including the topographic effects. In their study, similarly to Teillet et al. (1985), they developed other two cosine-based normalization methods which used the obtained coefficients of linear regression:

$$\sigma^0_{ref} = \sigma^0_\theta \frac{cos^q(\theta_{ref}) + c}{cos^q(\theta_0) + c} \quad (9)$$

$$\sigma^0_{ref} = (\sigma^0_\theta - a)\frac{cos^q(\theta_{ref})}{cos^q(\theta_0)} + a \quad (10)$$

where *c = a / b*. With these normalizations, Hinse, Gwyn, Bonn (1988) was able to reduce only a maximum of 10 percent of variance caused by incidence angle, Bayer et al. (1991) reduced 5-13 % for forested areas and 5.5-12 % for agricultural lands, whereas Teillet et al. (1985) mentioned that simple cosine corrections on a general forest class show only a little or no significant improvement compared to uncorrected data and these methods marked as inadequate to correct the data, especially in places where incidence angles are greater than 50°. However, from the linear regression they got different coefficients for each class, what make the classes separable. Anyway, they suggest using terrain correction methods on data to get more reliable results in classification of forests.

In some researches (i.e. Bayer et al., 1991) the coefficients of linear regression were calculated using algorithm for least-squares estimation of nonlinear parameters.

1.5.2 Regression-based normalization

In most of the studies, in the process of removing the incidence or local incidence angle dependency on backscatter, all image values are normalized to the same incidence angle (Dostálová et al., 2016; Dostálová et al., 2018; Gauthier et al., 1998; Nguyen et al., 2015).

The prerequisite for successful application of the regression-based normalization is to find a clear relationship between backscatter and (local) incidence angle. Several studies used linear regression analysis to model this relationship (Dostálová et al. 2016; Gauthier, Bernier, Fortin 1998; Nguyen et al. 2015; Dostálová et al. 2018; Rüetschi, Schaepman, Small 2018; Widhalm, Bartsch, Goler 2018; Makynen, Karvonen 2017; Pathe et al. 2009; Mougin et al. 1995). For example, Teillet et al. (1985) experienced a statistically significant correlation between SAR backscatter and local incidence angle for different forests types and clearings. Pairman et al. (1997) supported this finding in their study, where the regression analysis between the backscatter values and local incidence angles showed a strong negative relationship. Mougin et al. (1995) using ERS-1 Wind Scatterometer C-band data observed a flat angular behaviour over tropical forests (regression line with slope b = 0.056) and shrub savannas (b = 0.089), while significant angular variations were observed for sparse vegetation (b = 0.13) and for bare surfaces (b = 0.21). In addition, in Frison & Mougin (1996) a higher slope for tree savanna (b = 0.12) was observed, and the Sahelian area (b = 0.15) and deserts (b = 0.24) were also investigated (fig. 2). Steeper regression lines were caused by a stronger influence of surface roughness and topography for these types of surfaces.

Fig. 2 Angular signatures of the backscattering coefficient for different vegetation types over Africa

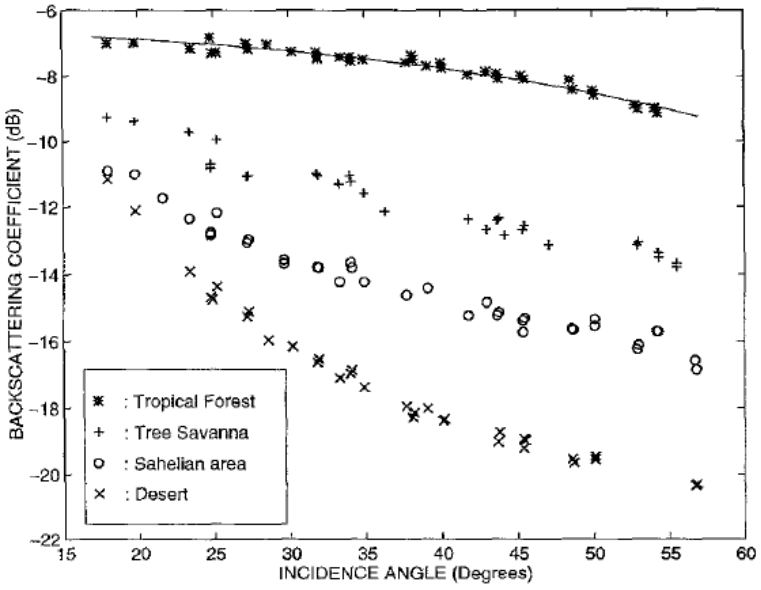

Source: Frison & Mougin (1996), p. 556

On the other hand, Hinse, Gwyn, Bonn (1988) experienced a weakly correlated result with a slight negative slope over forested areas, though the correlation was statistically significant. The source of the weak correlation could originate from the fact that they calculated the linear regression between backscatter and cosine of the incidence angle instead of the original incidence angle value. They found that for pixels with slopes less than 6° and at local incidence angle less than 26° did not occurred any clear correction after the correction using semi-empirical cosine-based methods. However, they found that pixels with higher slope angles have a stronger correlation to the backscatter value.

According to Pairman et al. (1997), noisy appear of scatter plots representing backscatter-incidence angle relationship at lower incidence angles is caused by several factors:

- Speckle noise is greater in the brighter areas
- Lower accuracy of the Digital elevation model (DEM) and possible errors in registration in areas with steep and rough terrain can be reason of error generation (mainly in areas with small local incidence angle)
- Possibility of less homogenous vegetation cover in areas with higher terrain variations

Elimination of backscatter-incidence angle relationship

The backscatter-incidence angle relationship can be generated in various ways. Nguyen et al. (2015) used a regression-based incidence angle correction allowing combination of observations from several tracks and years. They used a pixel-based method, where they used all available images from the time range from January 2007 till December 2011 to compute the regression line for each image pixel separately, so for each pixel they received a specific slope and offset parameter of the regression line. The number of observation used for a regression line generation was based on the spatial extent of overlapping images used for it in the selected time range (the average number of measurements for a pixel was 101), while the number of different tracks was only 15 in total. In this case, using multiple acquisitions from the same path through the year, a range of different backscatter values can be generated for a certain incidence angle, which is caused mainly by the different growing season of plants or by the changing climatic conditions during the year (as in fig. 3).

The same pixel based method was used also in Widhalm et al. (2018), where they determined the linear relationship of incidence angle and backscatter for mapping land cover types in high latitude environments based on time series of Sentinel-1 data. This method was used also for analysing the annual variation of forest backscatter (Dostálová et al., 2016) and for annual seasonality monitoring of forests and their type classification using Sentinel-1 data (Dostálová et al., 2018). It was successfully used also in a surface soil moisture retrieval approach over Oklahoma, USA using between 120 and 190 measurements for each pixel (Pathe et al. 2009).

Fig. 3 Relationship of incidence angle and backscatter for a selected area plotted for several measurements over a long period of time.

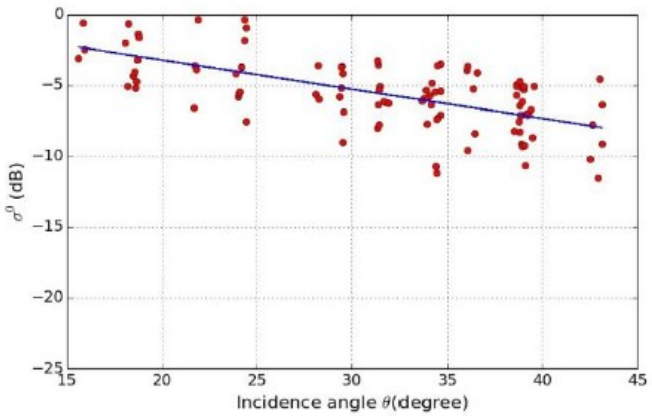

Source: Nguyen et al. (2015), p. 15876

On the other hand, in Widhalm et al. (2018) the relationship of incidence angle and backscatter was estimated from several flight tracks, too, but based on the specific land cover type, so for each land cover type in the study they had specific coefficients of regression. They called this method as slope approach. Loew et al. (2006) also derived the angular dependency of backscatter from only image pixels from a specific land-use class using 67 ENVISAT ASAR WSM images. The incidence angle range was then divided to steps of 5° and mean values was calculated for each step.

After the finding of the relationship between LIA and backscatter calculation of regression parameters, the next step is to apply an elimination of this relationship. In these studies, each scene was corrected to the same reference incidence angle θ_{ref} using the equation, thus eliminating the effect of different radar incidence angle:

$$\sigma^0_{ref} = \sigma^0_\theta - b\ (\theta - \theta_{ref}) \quad (11)$$

where σ^0_θ is the backscatter value at his original incidence angle θ, b is the slope of the linear regression line and θ_{ref} is the reference incidence angle, to which the resulted backscatter is going to be corrected.

This equation was using radar incidence angle θ was used in several studies, tough with different reference incidence angles, usually using the middle value of the radar incidence angle range and (Dostálová et al. 2016; Gauthier, Bernier, Fortin 1998; Nguyen et al. 2015; Dostálová et al. 2018; Rüetschi, Schaepman, Small 2018; Widhalm, Bartsch, Goler 2018; Makynen, Karvonen 2017; Pathe et al. 2009).

In some studies, the linear relationship between the local incidence angle and backscatter was calculated in other ways. For example, Gauthier et al. (1998) calculated the linear regression for the selected test sites on image pairs acquired from opposite orbits. Differences in backscatter values and in local incidence angles for test sites in each image pair were chosen as dependent and independent variables, respectively. Makynen & Karvonen (2017) calculated the dependence of differences in incidence angle and in backscatter of Sentinel-1 EW image pairs acquired in ascending and descending orbits over the same area covered by sea ice.

1.5.3 Radiometric terrain correction – Terrain Flattening

Radiometric Terrain Correction (or Terrain Flattening - TF), developed by Small (2011) is currently the most know and most used method for removing the influence of terrain on backscatter values. Using this method, not only the geometry, but also the radiometry of the scene is corrected for the terrain influences (Rüetschi, Small, Waser 2019). In this method, the accurate knowledge of the acquisition geometry of image geometry and a DEM is used to estimate the local illuminated area of each image pixel (Small 2011). Local illuminated area is then used to normalize the backscatter value instead of LIA. Beta nought (β^0) is converted to the so called gamma naught convention (γ^0) (Small 2011).

This method is implemented in Sentinel-1 Toolbox of the SNAP software and as input bands requires non-ortho-rectified corrected data, because local incidence area can be derived only from the azimuth and slant range pixel spacings, and a DEM, while the output is the terrain flattened γ^0.

1.5.4 Other methods

In the available literature, some other methods were also used. For example, Bouvet & Le Toan (2011) in their rice mapping methodology overcame the effect of different incidence angles caused by different sensing tracks with the "rationale" method. In this method, all two consecutive image pairs from the same track were used to derive the ratio of backscatter between the two images for each pixel. As a result, they obtained comparable images from different tracks from which created a classification feature for a classification. This classification was based on the maximum value of these images among each rice growing season. The selection of the maximum value assumes that the backscatter increases during rice growing season and over other land cover classes it is relatively stable.

Topouzelis & Singha (2016) compared three different types of incidence angle normalizations for oceanographic applications: 1) the cosine square normalization, 2) theoretical backscattering shape function derived from a minimum wind speed and 3) empirical range fit.

The last two assume of linear relationship between the incidence angle and backscatter value and use the inverse function (symmetric function to the linear function describing that relationship) to reverse the extracted linear profile. Then the normalization (14) is calculated as the average of the original (12) and symmetric functions (13).

$$\sigma_\theta^0 = b\theta + a \quad (12) \qquad (\sigma_\theta^0)^{-1} = b\theta + 2b\theta_{ref} + a \quad (13) \qquad \sigma_{\theta ref}^0 = \frac{\sigma_\theta^0 + (\sigma_\theta^0)^{-1}}{2} \quad (14)$$

The so-called histogram-based equalization belongs to the methods based on statistical techniques. Its main advantage is, regarding to Mladenova et al. (2013), in that it can explains the nonlinear relationship between backscatter and local incidence angle and it is not sensor or site specific.

In the study of Bayer et al. (1991) the simple backscatter mean value model of the local incidence angle produced similarly good results as the polynomial or cosine-based models.

Another way is to use additional auxiliary data in addition to the DEM for eliminating the topographic effects. For example, Franklin et al., (1995) used also red

and near-infrared bands of Landsat and SPOT optical sensors to estimate the forest canopy depth.

1.6 Seasonality vs short-term variations in radar backscatter

When analysing time series generated from satellite data, it is necessary to distinguish between various random short-term (e.g. rainfall) and seasonal variations (e.g. phenological phase). In optical data, seasonal effects are manifested by a change in the phenological phase due to the strong seasonality in photosynthetic activity, such as in the NDVI index. Time series from radar data do respond to the phenological phase differently – by the change in the structure of the tree crown and a by the change in the moisture (Ulaby, Moore, Fung 1981). Increase of the humidity of the object or change in structure may cause the reflectance value to skew.

1.6.1 Seasonality in forest backscatter response

Dostálová et al. (2016), using Sentinel-1 C-band time-series, showed a yearly variation in backscatter over forests to be between 1 and 3 dB, where coniferous forests showed significantly higher values with different seasonal behaviour compared to deciduous forests. This made the two types clearly separable for the classification. In other study, Dostálová et al. (2018) observed a clear difference in seasonal variation of herbaceous and woody vegetation using C-band Sentinel-1 time-series. Within woody vegetation, the deciduous forests showed an easily distinguished backscatter from coniferous forests and vineyards, which had very similar responses between each other. Easily distinguished seasonal variation of backscatter over deciduous forests has been also shown in Guccione et al. (2016).

Frison et al. (2018) found that the ratio of VV and VH polarization shows clearer seasonality over deciduous forests compared to VV polarization alone, where no seasonal variation was found, and VH, where slight variation was observed. They also showed a great correlation between backscattering coefficient ratio and deciduous forest's phenology measured by NDVI profiles from Landsat-8 data. This also proved the sensitivity of C-band signal to the upper layer of the forest canopy, especially to leaves and primary branches. In contrast, coniferous forest did not show an apparent seasonality in radar backscatter in their study, however in the NDVI profile did. Authors

attributed that seasonality to the understory vegetation composed of deciduous species which can contribute to the nadir-pointing optical sensor's reflectivity. Moreover, results of this study indicate that the phenology of vegetation can be estimated with higher accuracy using Sentinel-1 C-band data compared to optical data.

That study confirmed the results of the study by Proisy et al. (2000) where the VV polarized C-band ERS data was marked as not suitable for monitoring seasonal variations of backscatter over mixed deciduous forests. According to authors, seasonal variations showed a chaotic behaviour, which they attributed to a strong backscatter response of branches in the beginning and the end of the leafy cycle. However, in their study, a time-series of data containing 45 images for a 3 year-long period was used, which refers to approximately 15 images per year. The resulted chaotic time-series variability can be therefore attributed to short-term variations of environmental effects or effects connected with changing growing cycle, which is not possible to capture in data with such a low temporal resolution. Another limitation of this study was the analysis of only one polarization, the VV polarization, whose low seasonal response over deciduous forests was observed also in recent studies using Sentinel-1 data (Frison et al., 2018).

Sharma et al. (2005) examined the backscatter from different forest types compared to open areas using 97 Radarsat C-band images from period 1996-2004. They found that short-term environmental variations have a great influence on backscatter acquired over forests and noticed that using only one image can lead to erroneous interpretation of the data. For example, soil moisture has more significant impact on open areas than for forest canopy, causing difficulties in separability of these classes if the soil moisture is high, where open areas can have similarly high backscatter as forests. On the other hand, wet snow can be useful in separability of these classes, because wet snow reduces the backscatter from open areas while from forests remain almost unchanged (caused by attenuation of signal by forest canopy).

1.6.2 Short-term variations in radar backscatter and their elimination

Short-term variations can cause variation in time series analysis. Therefore, in some studies, there was an attempt to eliminate these variations. One of the methods is using temporal averaging of the resulting images to smooth the time series curve to reduce random noises (Dostálová et al., 2016; Dostálová et al., 2018; Nguyen et al., 2015).

Among the disadvantages we can list the possible generation of noise caused by changes in land cover or shifts in the change detection caused by narrower range of observations. Despite of disadvantages of this method, Nguyen et al. (2015) stated that a weekly sampling of rice fields is enough for capturing any change, so they choose a 7-day interval to calculate the mean of backscatter over all acquisitions. The 7-day interval was chosen also to tackle the temporal heterogeneity of the Envisat acquisitions. By that they created a more smoothed, but temporally reduced time series based on original data. Based on this work, Dostálová et al. (2016) and Dostálová et al. (2018), in an effort of eliminating of environmental effects and noise, calculated 12-day averages from the time series and then applied a Gaussian temporal filter to even more limit these noise causing effects.

Reiche et al. (2018) wanted to find out how the spatial normalization, created using optical data in their previous study (Hamunyela et al. 2016), reduces seasonal effects and how these effects affect time series generated from Sentinel-1 C-band (in VV polarization) compared to Landsat NDVI and PALSAR L-band (VH polarization) time series. They found that seasonality was most evident in the optical data (Landsat) and for Sentinel-1 and PALSAR data, the seasonal backscatter effects were much smaller, and the class separability results can be improved by normalization (significantly for the Sentinel-1 data).

2 Study areas, data, and methods

2.1 Study areas

The selection of study areas was limited to four Central European countries - Czechia, Slovakia, Hungary, and Poland (fig. 4). This study deals with 15 study areas - 10 with majority of the coniferous forests and 5 with majority of the broadleaf forests. Each study area was defined as a 20x20 km bounding box around a central point. The main criteria for the selection of the study area was that the share of forests (according our forest mask) must be higher than 50%. Exception was given to study area 8, which share of the forests was only 26%, because we wanted to include also broadleaf forests in lowlands with mean elevation lower than 150 m a.s.l. In similar areas the share of forests is usually very low in the Central Europe – the majority of the areas are represented by agricultural lands. These areas had to represent areas with majority of coniferous or deciduous forests in national parks (NP) or protected landscape areas (PLA) at various elevations, and with different slope values (tab. 2). Selection of protected areas was motivated by our long-term research interest in forest monitoring in Czech and Slovak national parks (Štych et al. 2019; Lastovicka et al. 2020; Stych et al. 2019).

For further testing of effectivity of the proposed method on short-term time series, central points of four study areas (1, 4, 6 and 12) with different LIA ranges were selected. Around these point a 20 m buffer was created (hereafter referred to as “case studies”). The main criterion in the selection of these case studies was that these areas had to be stable – were not significantly disturbed by anthropogenic or environmental factors in the time range 2015-2020. For these case studies, various characteristics were calculated – elevation, slope and aspect values and LIA range with minimum and maximum values (tab. 3).

Fig. 4 Map of study areas

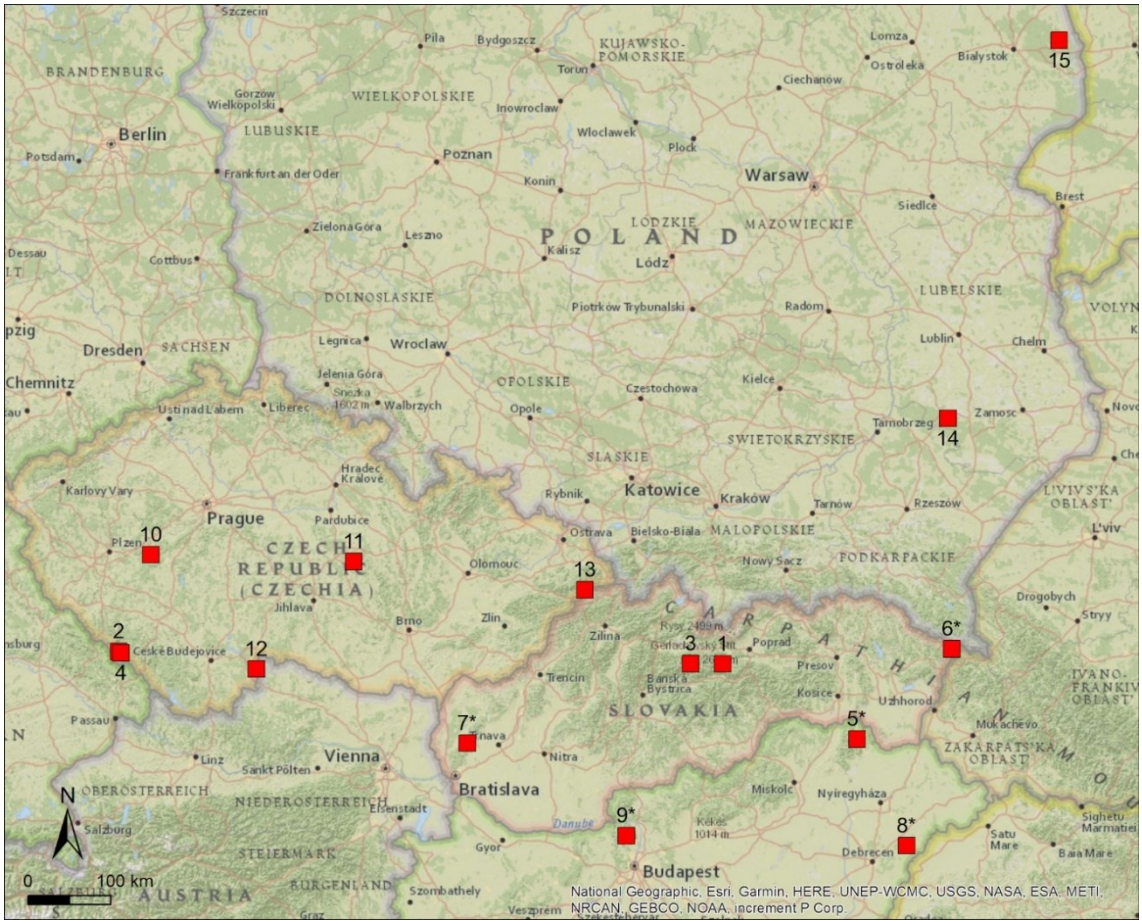

Explanatory notes: study areas marked with * are broadleaf forests

Tab. 2 Characteristics of study areas

Study area	Coordiates of the central point (x, y)	Mean elevation (m a.s.l.)	Mean slope (degrees)	Description
1	20.0088, 48.9569	1098.24	18.44	Coniferous forest in the Low Tatras NP (SK)
2	13.4776, 49.0457	1044.99	9.17	Coniferous forest in the Šumava NP (CZ)
3	19.6625, 48.9596	1133.66	22.54	Coniferous forest in the Low Tatras NP (SK)
4	13.5026, 49.0347	1058.60	8.77	Coniferous forest in the Šumava NP (CZ)
5*	21.4618, 48.4200	334.76	11.61	Broadleaf forest in Zempléni mountains PLA (HU)
6*	22.4873, 49.0644	714.49	15.94	Broadleaf forest in Poloniny NP (SK)
7*	17.2490, 48.3916	357.66	9.12	Broadleaf forest in Malé Karpaty PLA (SK)
8*	21.9982, 47.6490	148.47	2.73	Broadleaf forest in Hajdúsági PLA (HU)
9*	18.9683, 47.7215	276.74	9.34	Broadleaf forest in Duna-Ipoly NP (HU)
10	13.8272, 49.7284	597.96	6.31	Coniferous forest in Brdy PLA (CZ)
11	16.0196, 49.6786	679.14	5.69	Coniferous forest in Žďárské vrchy PLA (CZ)
12	14.9671, 48.9217	508.58	4.35	Coniferous forest in Třeboňsko PLA (CZ)
13	18.5186, 49.4805	722.35	15.27	Coniferous forest in Beskydy PLA (CZ)
14	22.4457, 50.6717	287.31	3.01	Coniferous forest in Lasy Janowskie PLA (PL)
15	23.6494, 53.1920	52.83	2.66	Coniferous forest in Knyszyn Forest NP (PL)

Source: Own work. Explanatory notes: study areas marked with * are broadleaf forests. PLA - Protected Landscape area, NP - National Park.

Tab. 3 Characteristics of case studies for use in the short-term time series analysis

Study area	Coordinates (x, y)	Elevation (m a.s.l.)	Slope/Aspect (degrees)	LIA range (max-min) in degrees
1	20.0088, 48.9569	1106	31 / 250	69 (72-3)
4	13.5026, 49.0347	994	18 / 292	36 (21-56)
6*	22.4873, 49.0644	562	13 / 170	22 (33-55)
12	14.9671, 48.9217	508	5 / 260	13 (33-45)

Source: Own work. Explanatory notes: case study marked with * is a broadleaf forests.

2.2 Google Earth Engine

For accessing and analysing data, and developing methods, Google Earth Engine (GEE) (https://earthengine.google.com), "a cloud-based platform for planetary-scale geospatial analysis that brings Google's massive computational capabilities" (Gorelick et al. 2017), was used. GEE was designed to help researchers easily spread they results to other researchers, policy makers, NGOs, field workers and to the public. GEE is accessed and controlled through an Internet-accessible application programming interface (API) and a web-based interactive development environment (IDE) that enables quick prototyping and visualization of results, so users can access data and perform analysis trough any web browser. (Gorelick et al. 2017)

Using GEE, there is no need to download gigabytes of data, because it contains "multi-petabyte" analysis-ready data including massive amount of satellite and aerial data from optical and radar wavelengths, environmental variables, weather and climate data, land cover datasets, topographic and socio-economic datasets. There is a possibility for users to make requirements on new datasets, so by the time the number of datasets is enlarging and are supplemented. Users can also use their own data (both raster and vector) and upload it directly to the GEE.

There is no need to download any software and having a computer with robust computation power. GEE has more than 800 in-built functions, representing the range from simple mathematical functions to powerful geostatistical and image processing operations. These functions are available using client libraries in Python or JavaScript languages. In addition, users can create their own algorithms. As all the computational power of the GEE is located in the "cloud", for access the data and functions is enough to have a web browser. All the work can be done directly in the web browser on the Earth Engine Code Editor available at code.earthengine.google.com (fig. 5).

Another great positive side of using GEE is that there is a large community of users who can share their ideas, ask for help, or ask questions about any kind of problem. Moreover, a huge archive of solved issues is available for everyone, thus bringing GEE closer to the general public.

Fig. 5 Earth Engine Code Editor

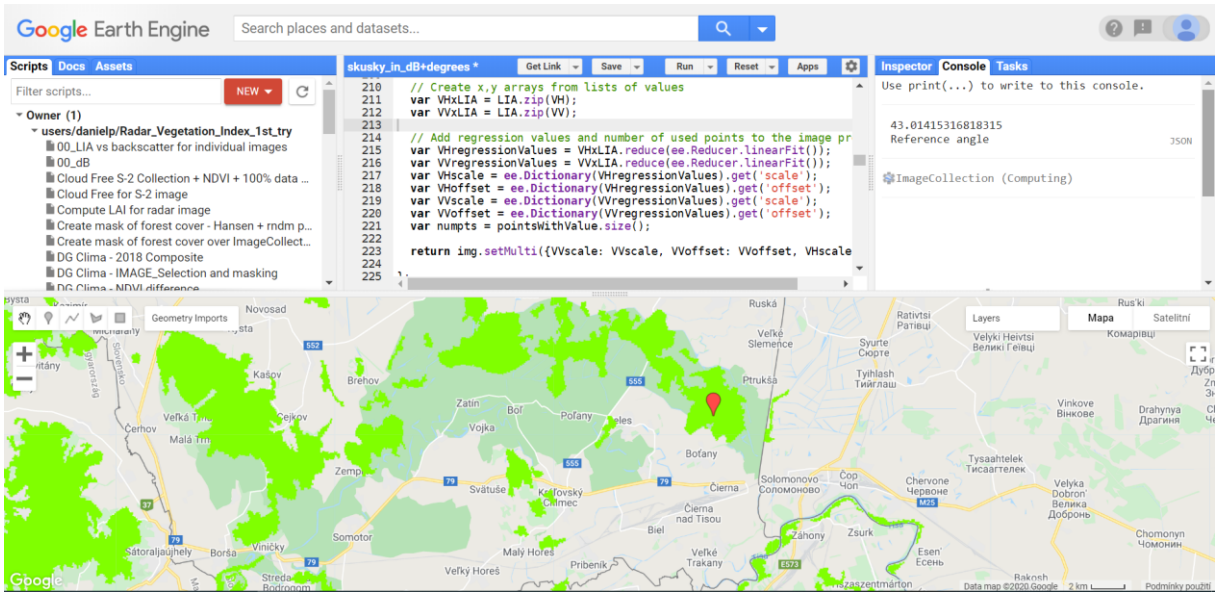

Note: For more information about Earth Engine Code Editor see developers.google.com/earth-engine/playground.

2.3 Data

2.3.1 Sentinel-1

The main data source for this study is represented by the Sentinel-1 SAR data. Sentinel-1 satellite family represents the continuation of earlier C-band spaceborne radar sensors of the ERS-1, ERS-2 and Envisat ASAR missions of the European Space Agency (ESA). The Sentinel-1 is the first series which was designed to meet the requirements of the Earth Observation of the European Union (EU). Sentinel-1 mission is based on systematic global coverage monitoring, proposed to monitor marine environment, including oil spill detection and sea-ice monitoring, mapping of land surfaces and mapping in support of crisis situations (natural disasters and humanitarian aid) (Torres et al., 2012).

The Sentinel-1 mission is composed of a constellation of two satellites, Sentinel-1A and Sentinel-1B, sharing the same orbital plane. A lifetime of one satellite is estimated to be between 7 up to 12 years. Satellites operate at C-band, at the centre frequency of 5.405 GHz, orbiting in a near Polar Sun-Synchronous orbit at a height of 693 km, having 12-day repeat cycle per satellite.

Sentinel-1 operates in four acquisition modes: Stripmap (SM), Interferometric Wide swath (IW), Extra-Wide swath (EW), Wave mode (WV), illustrated in fig. 6. For the detailed information see tab. 4 and fig. 6. Compared to ERS satellites or other SAR sensors, which primarily acquire data in a StripMap mode (line by line), Sentinel-1 data are acquired in TOPS mode (neighbouring pixels are of different acquisition phases). Compared to other existing C-band SAR systems (ASAR/Envisat or RADARSAR-2), in the case of Sentinel-1 great attention was focused on the radiometric accuracy. An absolute radiometric calibration is only 1 dB (3σ) of all acquisition modes with radiometric stability of 0.5 dB (3σ). Noise Equal to Sigma Zero (NESZ) for Sentinel-1 is -22dB.

The main acquisition mode is the IW mode with 250 km wide swath, with high geometric (5m in ground range x 20 m in azimuth resolution) and radiometric resolution operates over the majority of the Earth's surface and acquiring images at VV or VV and VH polarization (fig. 7 and fig. 8). The EW mode with a 400 km wide swath is operates mainly over polar areas including seas and acquiring images at HH or HH and HV polarizations (fig. 7 and fig. 8). The incidence angle in IW mode has a range from 31° to 46°, while the EW mode from 20° to 47°.

Except for WV mode, which is using a single polarization (HH or VV), imaging instruments of Sentinel-1 support dual polarization (HH + HV or VV + VH) at each acquisition mode, using one transmit chain (H or V) and two parallel receiver chains for H and V polarization. (Torres et al. 2012)

Tab. 4 Characteristics of Sentinel-1 acquisition modes.

Parameter	Interferometric Wide-swath mode (IW)	Wave mode (WV)	Strip Map mode (SM)	Extra Wide-swath mode (EW)
Polarisation	Dual (HH + HV, VV + VH)	Single (HH, VV)	Dual (HH + HV, VV + VH)	Dual (HH + HV, VV + VH)
Access (incidence angles)	31°–46°	23°–37° (mid incidence angle)	20°–47°	20°–47°
Azimuth resolution	<20 m	<5 m	<5 m	<40 m
Ground range resolution	<5 m	<5 m	<5 m	<20 m
Azimuth and range looks	Single	Single	Single	Single
Swath	>250 km	Vignette 20×20 km	>80 km	>410 km
Maximum NESZ	−22 dB	−22 dB	−22 dB	−22 dB
Radiometric stability	0.5 dB (3σ)	0.5 dB (3σ)	0.5 dB (3σ)	0.5 dB (3σ)
Radiometric accuracy	1 dB (3σ)	1 dB (3σ)	1 dB (3σ)	1 dB (3σ)
Phase error	5°	5°	5°	5°

Source: Torres et al. (2012), p. 13

Sentinel-1 products are accessible in different processed levels. SAR raw data are represented with data Level-0, from which Level-1 data are generated. Pre-processed Level-1 include two categories: Single Look Complex imagery (SLC) mainly for interferometric applications and Ground Range Detected Georeferenced imagery (GRD) for intensity-based applications. (Torres et al. 2012)

Level-1 SCL products contain pixels represented by a complex (I and Q) magnitude value containing both amplitude and phase information. Coordinates of image plane are preserved in the original dimensions: slant range by azimuth. These images contain three sub-swaths per polarization, resulting in 6 images in total for IW mode. In the SM and WV modes the image pixel spacing are preserved at the natural spacing, while in IW mode, the image is resampled to a common pixel spacing grid in range and azimuth.

Level-1 GRD images are derived products from SCL, having the slant range coordinates projected onto the ellipsoid of the Earth and pixel values represent the detected magnitude, while phase information is lost. Each image burst was multi-looked, so the speckle was reduced, and then the bursts were seamlessly merged into single image per polarization channel.

Fig. 6 Acquisition modes of Sentinel-1

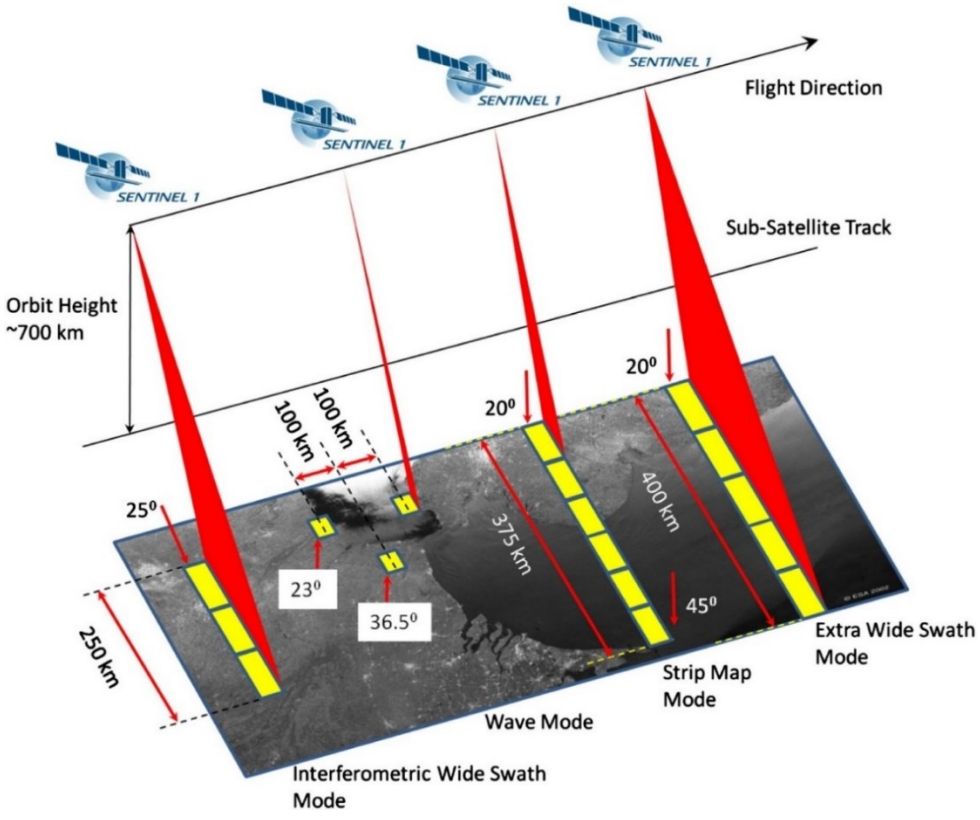

Source: adopted from Torres et al. (2012), p. 13

Fig. 7 Sentinel-1 revisit & coverage frequency

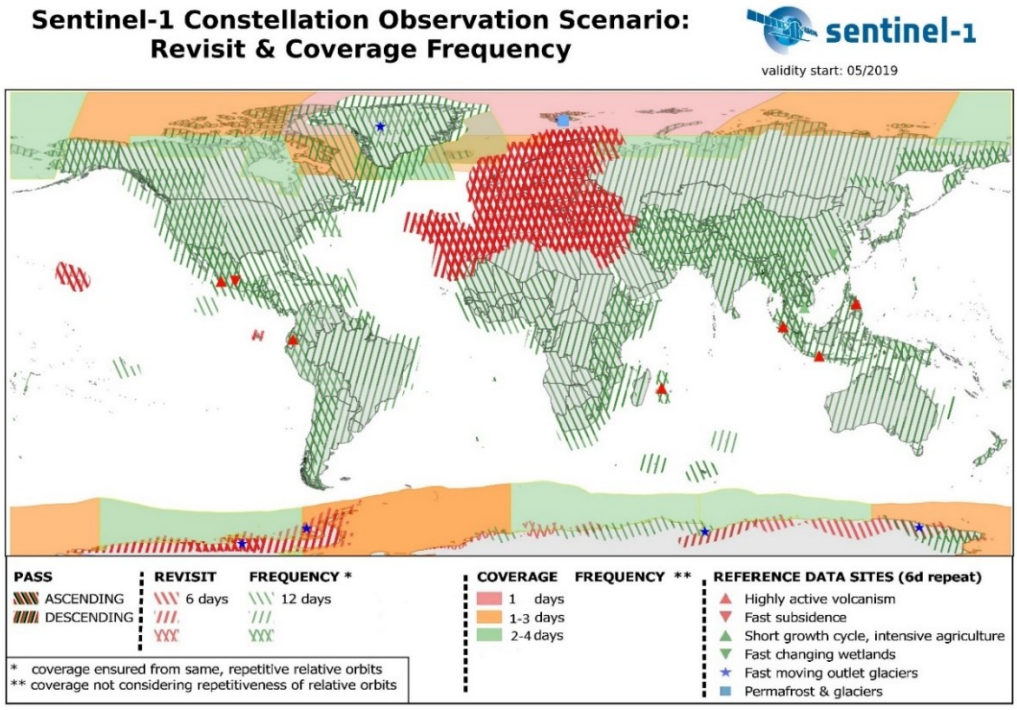

Source: ESA (2020)

Fig. 8 Sentinel-1 mode, polarization, and observation geometry

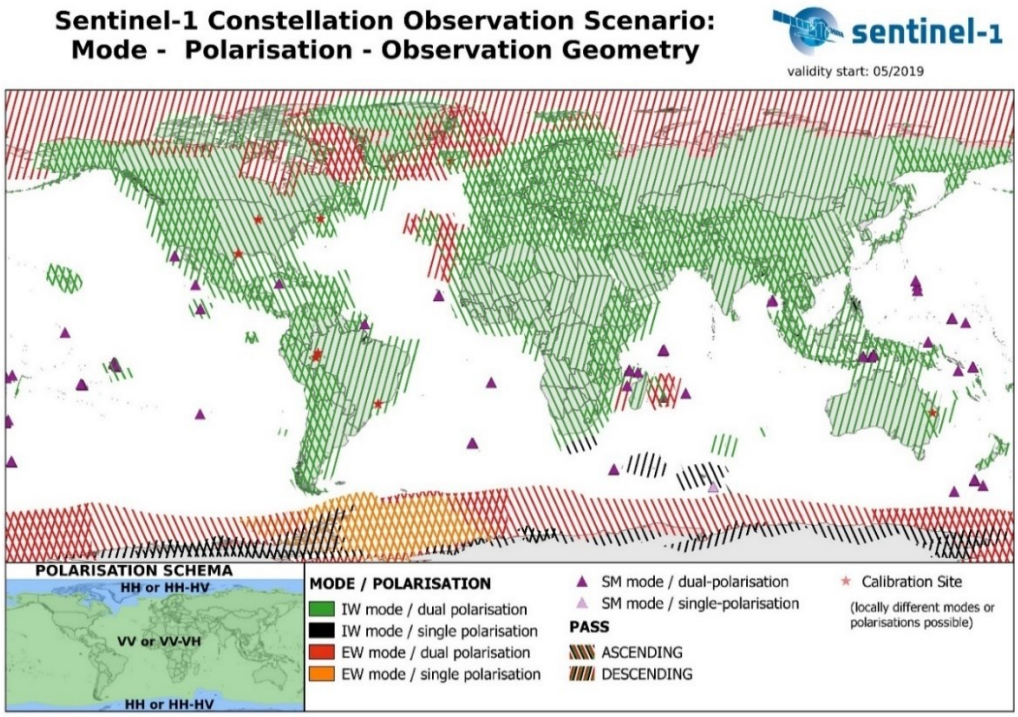

Source: ESA (2020)

Sentinel-1 data in Google Earth Engine

In our study Sentinel-1 Level-1 GRD scenes were used, which are available in GEE. Sentinel-1 images in GEE were pre-processed to backscatter coefficient σ°. The σ° represents target backscattering area (radar cross-section) per unit ground area processed to backscatter coefficient σ° converted to decibels as $10*\log_{10}\sigma°$. Pre-processing of scenes in GEE was performed using the SNAP Sentinel-1 Toolbox and included the following steps: applying the orbit file, GRD border noise removal, thermal noise removal, radiometric calibration, terrain correction (orthorectification) using the SRTM 30-meter DEM or the ASRER DEM for high latitudes (>60° or <-60°). The most used method for correction of different backscatter values caused by terrain, the so-called Radiometric Terrain Flattening, was not applied in GEE due to artifacts on mountain slopes. (GEE 2020b).

2.3.2 Digital terrain model SRTM

Another important input data was the Digital terrain model Shuttle Radar Topography Mission (DEM SRTM) which was born based on the need of globally consistent topographic data using a consistent mapping technique. The so-called interferometric SAR (InSAR) technique was used, where phase difference of two radar images acquired with a very small base to height ratio (0.00002) was used to measure the topography. In this mission, bands X and C were used. As the data acquisition was done using radar, the return of the signal could be influenced by the vegetation, especially by their height, structure, and density. Dense vegetation did not allow the penetration of the signal to the ground base, so the data represents their height, while clear-cuts in dense forests are clearly noticeable. On the other hand, very smooth surfaces such as calm water, steep slopes facing away the radar (causing shadowing) or toward the radar (foreshortening or layover) may not scatter enough energy back to the sensor, thus causing areas of extreme errors – voids. (Farr et al. 2007)

The database in GEE (SRTM V3 product (SRTM Plus) provided by NASA JPL), in contrast to earlier versions, undergo a void-filling process using open-source datasets such as ASTER GDEM2, GMTED2010, and NED. Data are available in 1 arc-second resolution, which corresponds to approximately 30 meters. (GEE no date)

According to the accuracy assessment, data achieved a height accuracy from 7 to 13 meters depending on continent (for Eurasia it is 8.8 meters) and an absolute vertical

accuracy of data was better than 9 meters (Farr et al. 2007). Santillan & Makinano-Santillan (2016) compared the height accuracy of models made from SRTM, ALOS and ASTER. They explored a territory in the Philippines, where altitudes ranged from 0 to over 2600 m. m. They found that SRTM achieved better mean error results in their case compared to previous studies - they found a mean error of 6.91 m, a standard deviation of 4.57 and a Root Mean Square Error (RMSE) 8.28 (mean error of 10 m and RMSE 16 m was expected).

2.3.3 Land Cover Databases

In this study, two land cover databases were used as complimentary data, the CORINE Land Cover (CLC) and Hansen et al.'s Global Forest Change databases.

CORINE Land Cover Database

CORINE CLC is a land cover inventory initiated in 1985 including five subsequent databases (CLC1990, CLC2000, CLC2006, CLC2012 and the latest CLC2018). The datasets were created by classification of satellite images with in-situ measurements used as ancillary data at a national level by national teams coordinated by the European Environment Agency (EEA). All the databases have are the same in the definition of main technical parameters: the minimum mapping unit (MMU) was set to 25 hectares, minimum width of linear element (MMW) to 100 metres, and the database nomenclature includes 44 land cover classes grouped in a three-level hierarchy. Although these classes were preserved though the time, their definition was changed (see Kosztra et al. 2019). Data processing methodology have been also changed. While the first CLC database was created using photointerpretation methods (hand-drawing of polygons and later digitised) which generated several errors, from the CLC2000 database the computer-assisted image interpretation (CAPI) was applied.

In our study we used the CLC2018 product, so we have added more detailed information for that product. The dominantly used satellite data presented Sentinel-2 imagery with Landsat-8 data used for gap filling. The geometric accuracy of CLC data was better than 100 m a thematic accuracy achieved results of ≤ 85%. (Büttner et al. 2017)

According to the CLC2018 nomenclature, forests belong to the "Class 3: Forest and semi-natural areas" and within that to the sub-category "Class 3.1 Forests". This sub-

category is divided to three "three-level" category: *311 Broad-leaved forest, 312 Coniferous forest* and *313 Mixed forest*. In these categories, only trees higher than 5 metres were taken into consideration with at least 30% coverage of forest crowns. Based on their definition, the coniferous forest class includes areas, where coniferous forests represent at least 75 % of the formation. The same was applied to the broad-leaved forest, where 75 % of trees must belong to broad-leaved stands. From both of types of forest class definitions, the mixed-forest places areas were excluded, while this class is defined separately in the database and it was not used in our study.

Hansen Global Forest Change database

Hansen et al.'s Global Forest Change database represents a database of global tree cover extent, loss, and gain at a spatial resolution of 30 m, originally for the period from 2000 to 2012 (Hansen et al., 2013a), later accompanied by data from subsequent years. Trees were defined in this database as all vegetation taller than 5 m in height, which matches the minimum tree height definition in CORINE CLC. Forest loss was defined as change of forest stand, having at least 50 % of crown cover at Landsat pixel scale, to non-forest (~0 % crown cover), while forest gain represents the inverse situation, where the non-forest state changes to forest. Selective logging or the so-called thinning within forest stands were not included to the forest less definition. Till 2012 Landsat 7 Enhanced Thematic Mapper Plus (ETM+) scenes were used, pre-processed, and processed in GEE. Training data were derived from very high resolution (VHR) optical imagery such as Quickbird or existing tree cover layers derived from Landsat and MODIS data. Validation of results has been performed using 1500 control areas at a global scale. These amount of control areas were divided between four types of climatic domains (tropical, subtropical, temperate, and boreal) and the validation was performed also for these areas separately. For global scale, the results showed a 99.6% and 99.7% of overall accuracy, 88% and 74% for producer's accuracy and user's accuracy achieved 87% and 76% for forest loss and gain, respectively. For the temperate climate domain 258 validation areas were available. Overall accuracies were 99.3% and 99.7%, while producer's accuracy was 94% and 98%, and user's accuracy was 88% and 77% for forest loss and gain, respectively. (Hansen et al., 2013b)

GEE currently (May 2020) includes the 1.6 version of the database which includes global forest coverage till 2018, where several changes were done relative to the original 1.0 version: from 2013, Landsat 8 Operational Land Imager (OLI) data were

used; reprocessing of forest loss was done from 2011; the training data calibration; and input spectral features for the loss model were improved. (Hansen et al. 2018)

2.3.4 Software used in the study

For pre-processing of Sentinel-1 data in the desktop environment, the Sentinel-1 Toolbox version 7.0. of the SNAP (Sentinel Application Platform) software version 7.0. was used.

Graphic calculator application in GeoGebra was used to create several figures mainly in methodology part. GeoGebra is an online mathematic software with an easy-to-use interface available at https://www.geogebra.org/. Main applications include: Caclulator Suite, Graphic Calculator, Geometry, 3D Calculator, CAS Calculator, Scientific Calculator and Notes. It is an open source software freely available for non-commercial users.

Microsoft Excel for Microsoft 365 and Google Sheets was used to create tables and figures mainly in Results section.

2.4 Methodology

Methodologically, the first step was to find the necessary satellite images and ancillary data sources available in GEE. After that, it was necessary to calculate the local incidence angle (LIA) for each Sentinel-1 image pixel. After calculating the LIA, ascending, and descending databases were merged. In order to collect an adequate amount of data for calculation of linear relationship between backscatter and LIA, in each study area we generated 1000 random points. A 20 m buffer was created around these random points. At the same time, a forest mask was generated from the combination of CORINE CLC and Hansen Global Forest databases. For further analysis, areas completely inside the forest mask were selected, ensuring that only forest areas will serve as input data to regression analysis. These forest areas were overlaid with Sentinel-1 images and the and mean values of backscatter and LIA were extracted. From these areas, a scatterplot was created, and the linear regression equation was calculated. The slope of the linear regression line and the LIA value was selected for the final LIA correction. For statistical comparison of study areas and evaluation of the proposed method, the same LIA value was used for each study area – 38.5°. For a short-term time series analysis and comparison, a mean value calculated from the minimum and maximum LIA for the selected case study was used. After the LIA correction, accuracy assessment was done, and time series were created. Fig. 9 shows the basic procedure of the methodology. Appendix 2 is describing the digital attachment of this work, where the JavaScript codes of the algorithm and codes for the calculation of statistical parameters are available.

In the next section, the individual steps of the methodology will be described in detail.

Fig. 9 Methodology used in this work

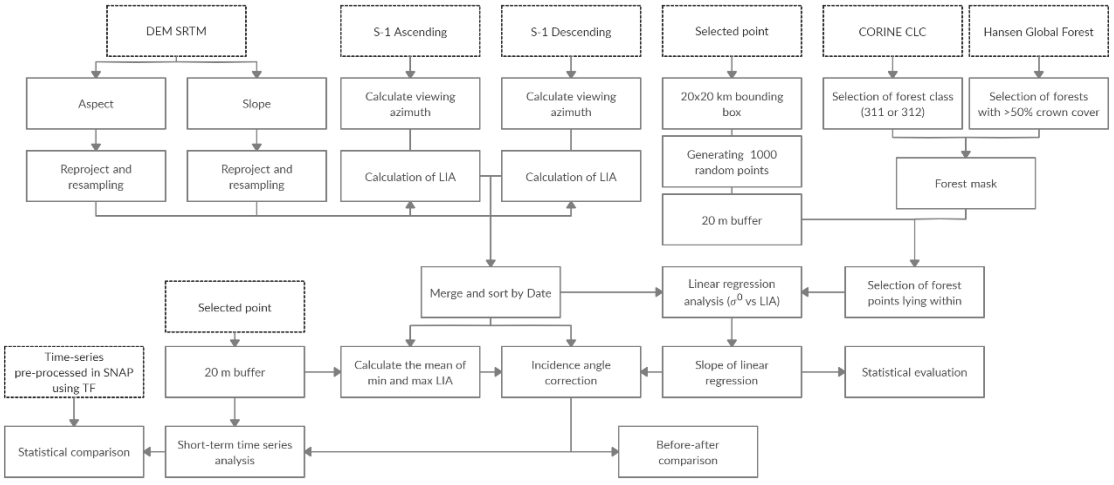

Source: own work

2.4.1 Calculation of local incidence angle

In the literature a clear definition of the local incidence angle can be found (Castel et al. 2001; Hinse, Gwyn, Bonn 1988; Franklin et al. 1995; Ulander 1996). Local incidence angle is the angle between the look vector *i* and the vector *n* normal to the surface, see fig. 10.

The calculation of the LIA requires knowledge of slope (α) and aspect angles (β) of the examined area and the viewing azimuth of the sensor (γ) (Radar Look Angle - RLA) (fig. 11). Slope and aspect were generated from SRTM DEM and then reprojected and resampled (using nearest neighbour method) to the Sentinel-1 band's projection and resolution grid, respectively. The viewing azimuth calculation was performed for each image separately, mainly because the ascending and descending pass have different viewing azimuths and therefore different LIA calculation method was needed.

Fig. 10 Difference between radar incidence angle (θ) and local incidence angle (θ_0)

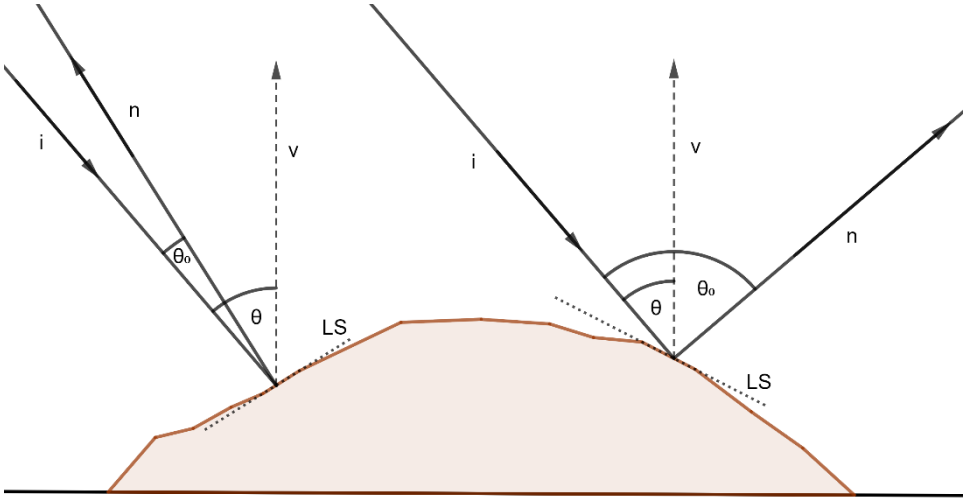

Source: own work based on Rizzoli, Brautigam (2014). Explanatory notes: i = look vector, n = vector vertical to the surface, represented by a local slope LS.

The derivation of the equation for calculation of LIA is based on a calculation of the distance of two vectors, where we assume two points lying on vectors *i* and *n*: point P_1 on vector *i* and point P_2 on the vector *n*. (fig. 11). These points have the same distance *k* from the point of contact with the surface *A*.

$$|P_1A| = |P_2A| = k \tag{15}$$

The distance we are going to calculate is the distance between points P_1 and P_2 – $|P_1P_2|$. For that, we need to define the coordinates x, y, z of points P_1 and P_2 using some basic trigonometric functions and then calculate the distance between them.

Fig. 11 Illustration of incidence wave vector *i* dependence on the vector normal to the surface *n* – angles and points involved in the computation of the LIA

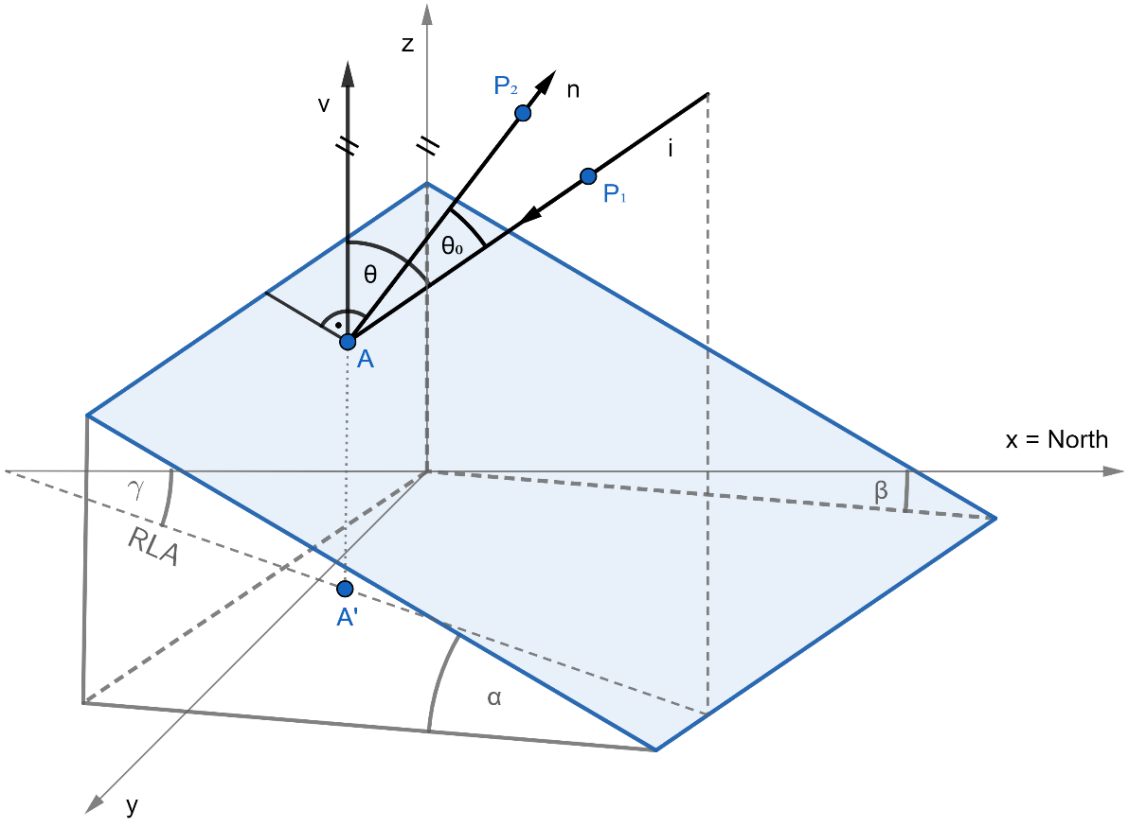

Source: own work based on Castel et al. (2001)

To define the *z* coordinate of points, we need to calculate it on the plane of incoming wave for P_1 (fig. 12) and on the plane of the vector normal to the surface for P_2 (fig. 13) using the following formulas:

$$\text{For } P_1\text{: } \cos\theta = \frac{z_1}{k} \Rightarrow\!\!\Rightarrow \boldsymbol{z_1 = k\cos\theta} \tag{16}$$

$$\text{For } P_2\text{: } \cos\alpha = \frac{z_2}{k} \Rightarrow\!\!\Rightarrow \boldsymbol{z_2 = k\cos\alpha} \tag{17}$$

Fig. 12 Incidence wave plane

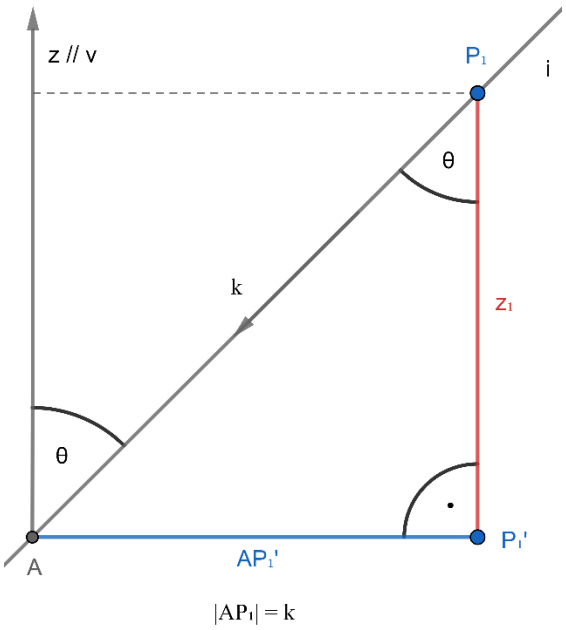

Source: own work

Fig. 13 Normal to the surface plane

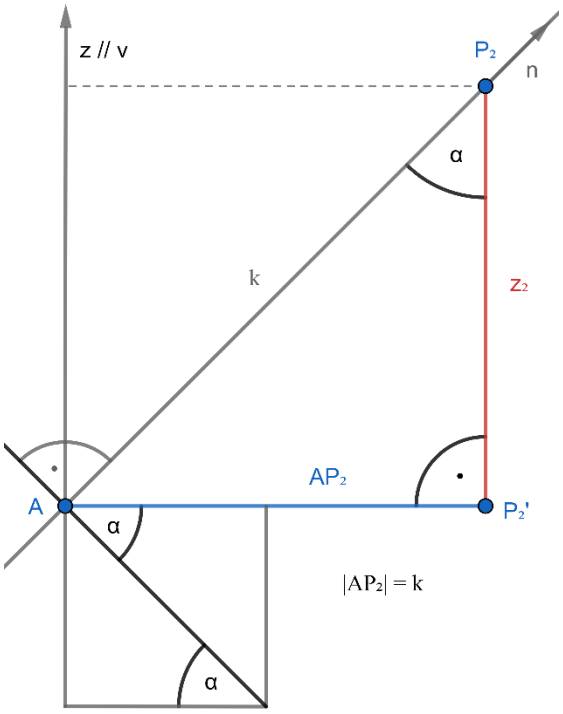

Source: own work

To define the *x* and *y* coordinates, we need to calculate the distances AP_1' and AP_2':

$$|AP_1'| = \mathrm{k} \sin\theta \tag{18}$$

$$|AP_2'| = \mathrm{k} \sin\alpha \tag{19}$$

To define the *x* and *y* coordinates, we need to calculate them on *xy* plane. For calculating the coordinates of point P_1 to project the incidence wave to the *xy* plane (fig. 14 a) and for point P_2 to project the vector normal to the surface to the *xy* plane (fig. 14 b). Then we got the following formulas:

For point P_1:

$$x_1 = |AP_1'| \cos\gamma \;\; \Rightarrow\Rightarrow \;\; \boldsymbol{x_1 = k \sin\theta \cos\gamma} \tag{20}$$

$$y_1 = |AP_1'| \sin\gamma \;\; \Rightarrow\Rightarrow \;\; \boldsymbol{y_1 = k \sin\theta \sin\gamma} \tag{21}$$

For point P_2:

$$x_2 = |AP_2'| \cos\beta \;\; \Rightarrow\Rightarrow \;\; \boldsymbol{x_2 = k \sin\alpha \cos\beta} \tag{22}$$

$$y_2 = |AP_2'| \sin\beta \;\; \Rightarrow\Rightarrow \;\; \boldsymbol{y_2 = k \sin\alpha \sin\beta} \tag{23}$$

Resulting in P_1 and P_2 coordinates as follows:

$$\mathbf{P_1\ [k \sin\theta \cos\gamma\ ,\ k \sin\theta \sin\gamma\ ,\ k \cos\theta]}$$

$$\mathbf{P_2\ [k \sin\theta \cos\alpha\ ,\ k \sin\theta \sin\alpha\ ,\ k \sin\alpha]}$$

Fig. 14 Calculation of *x* and *y* coordinates on *xy* plane for P_1 (a) and for P_2 (b)

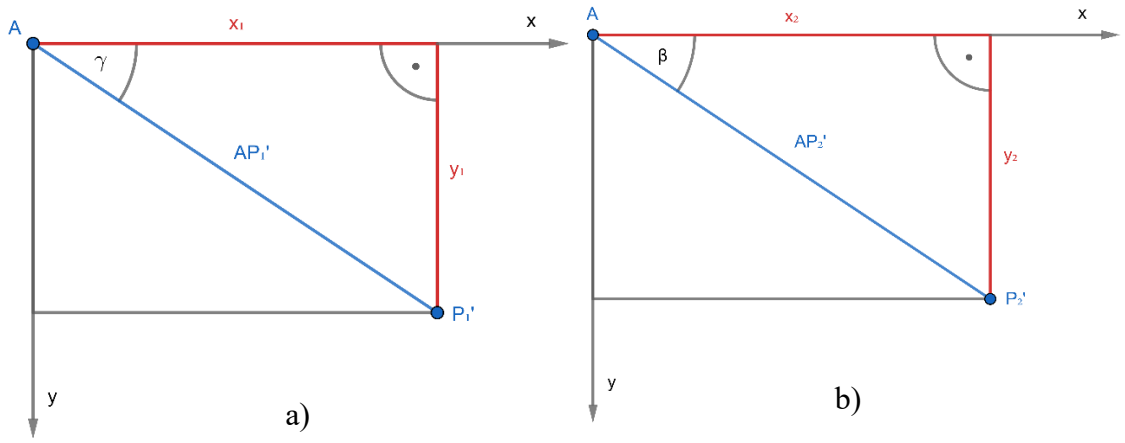

Source: own work. Explanatory notes: *AP_1' represents the projected incident wave to the xy plane, AP_2' represents the projected vector normal to the surface to the xy plane*

To get the distance between points P_1 and P_2 we can use the distance between two points P_1 and P_2 in a *xyz* space which is given by the following formula:

$$|P_1P_2| = \sqrt{(x_1 - x_2)^2 + (y_1 - y_2)^2 + (z_1 - z_2)^2} \tag{24}$$

after substitution of *x*, *y*, and *z* coordinates to the equation we got:

$$|P_1P_2| = k\sqrt{(\sin\theta\cos\gamma - \sin\alpha\cos\beta\ )^2 + (\sin\theta\sin\gamma - \sin\alpha\sin\beta)^2 + (\cos\theta - \cos\alpha)^2} \tag{25}$$

$$|P_1P_2| = k\sqrt{\begin{matrix}\sin^2\theta\cos^2\gamma - 2\sin\theta\cos\gamma\sin\alpha\cos\beta + \sin^2\alpha\cos^2\beta + \\ +\sin^2\theta\sin^2\gamma - 2\sin\theta\sin\gamma\sin\alpha\sin\beta + \sin^2\alpha\sin^2\beta + \\ +\cos^2\theta - 2\cos\theta\cos\alpha + \cos^2\alpha\end{matrix}} \tag{26}$$

$$|P_1P_2| = k\sqrt{\begin{matrix}\sin^2\theta\,(\cos^2\gamma + \sin^2\gamma) + \sin^2\alpha\ (\cos^2\beta + \sin^2\beta) + \cos^2\theta + \cos^2\alpha - \\ -2\sin\theta\cos\gamma\sin\alpha\cos\beta - 2\sin\theta\sin\gamma\sin\alpha\sin\beta - 2\cos\theta\cos\alpha\end{matrix}} \tag{27}$$

where according to the Pythagorean formula for sines and cosines $\cos^2\gamma + \sin^2\gamma = 1$ and $\cos^2\beta + \sin^2\beta = 1$, and then $\sin^2\theta + \cos^2\theta = 1$ and $\sin^2\alpha + \cos^2\alpha = 1$, then we get a following equation for the $|P_1P_2|$ distance:

$$|P_1P_2| = k\sqrt{2 - 2\sin\theta\cos\gamma\sin\alpha\cos\beta - 2\sin\theta\sin\gamma\sin\alpha\sin\beta - 2\cos\theta\cos\alpha} \tag{28}$$

After that, we can calculate the angle between vectors *i* and *n* using the cosine formula for the AP_1P_2 triangle using the following equation:

$$\cos\theta_0 = \frac{|AP_1|^2 + |AP_2|^2 - |P_1P_2|^2}{2\,|AP_1|\,|AP_2|} \tag{28}$$

Where AP_1 and AP_2 are defined as *k*, so after the substitution to the equation we get:

$$\cos\theta_0 = \frac{2k^2 - |P_1P_2|^2}{2k^2} \tag{29}$$

following by some simplifications and substitutions:

$$|P_1P_2|^2 = 2k^2 - 2k^2\cos\theta_0 \tag{30}$$

$$\begin{aligned} k^2(2 - 2\sin\theta\cos\gamma\sin\alpha\cos\beta - 2\sin\alpha\cos\beta\sin\alpha\sin\beta - 2\cos\theta\cos\alpha) \\ = 2k^2 - 2k^2\cos\theta_0 \end{aligned} \tag{31}$$

$$2 - 2\cos\theta_0 = 2 - 2\sin\theta\cos\gamma\sin\alpha\cos\beta - 2\sin\theta\sin\gamma\sin\alpha\sin\beta - 2\cos\theta\cos\alpha \tag{32}$$

$$\cos\theta_0 = \sin\theta\cos\gamma\sin\alpha\cos\beta + \sin\theta\sin\gamma\sin\alpha\sin\beta + \cos\theta\cos\alpha \tag{33}$$

$$\cos\theta_0 = \cos\theta\cos\alpha + \sin\alpha\,sin\,\theta\,(\cos\gamma\cos\beta + \sin\gamma\sin\beta) \tag{34}$$

Where $cos\,\gamma\,cos\,\beta + sin\,\gamma\,sin\,\beta$ according to Ptolemy's identities can be simplified as $cos\,(\gamma - \beta)$ resulting in the final form of the equation:

$$\boxed{\cos\theta_0 = \cos\theta\cos\alpha + \sin\alpha\, sin\,\theta\, cos\,(\gamma - \beta)} \quad (35)$$

where θ_0 is the local incidence angle we are looking for, θ is the radar incidence angle, α is the local slope, β is the aspect angle of the terrain and γ is the viewing angle.

For that equation, there is an assumption that vectors *i* and *n* has the same direction, starting from the point of contact *A*. For that reason, we need to subtract 180° from the viewing angle γ to get that direction of the vector *I*, resulting in $\gamma = \gamma - 180°$.
The equation where the original direction of incidence angle is taken into account will look like that in Castel et al. (2001):

$$\boxed{\cos\theta_0 = \cos\theta\cos\alpha - \sin\alpha\, sin\,\theta\, cos\,(\gamma - \beta)} \quad (36)$$

2.4.2 Calculation of the viewing azimuth

For the resulted equation (36) we need to know the slope α and the aspect angle β of the area, radar incidence angle θ and the viewing azimuth of the sensor γ. Radar incidence angle θ is known for each pixel, it is available as a separate band in the Sentinel-1 GRD product. The slope α and the aspect β angles can be calculated from the SRTM DEM. However, the viewing azimuth can be different in different geographical locations. Therefore, it is necessary to calculate it for each individual scene separately. We need to calculate it for descending and ascending orbits, too.

For the calculation of the viewing azimuth for the ascending orbit we need to first calculate the flight azimuth of the satellite respective to the true north *N*. This can be done by finding the Southernmost *A* and the westernmost point *B* of the scene, which are points lying on the vector parallel to the flight direction vector. We can get the x and y coordinates of points *A* and *B* and calculate the distance between these points in x and y planes while we get a right triangle $\triangle OAB$, where *a* represents the distance of points *A* and *B* ($|A_yB_y|$) in the *y* plane, and *b* is their distance ($|A_xB_x|$) in the *y* plane. From $\triangle OAB$ it is possible to calculate the angle β, which is the angle between the near range of the image and the true north N (fig. 15). According to the goniometric functions for right triangles, β is calculated as

$$\beta = \arctan(b/a). \quad (37)$$

The angle between the true north N and the flight direction is represented by α as

$$\alpha = \beta + 270°. \tag{38}$$

The view direction is perpendicular to the flight direction, so in case of ascending orbit the viewing azimuth γ is calculated as

$$\gamma = \alpha - 270°. \tag{39}$$

As images acquired in the descending orbit of the satellite is rotated differently compared to ascending images, in that case it is necessary to find the southernmost A and easternmost B points of the scene. Find the distances of these points in the x and y planes $|A_xB_x|$ and $|A_yB_y|$, while creating a right triangle $\triangle OAB$ (fig. 16). The angle β between the near range of the image and the true north N is calculated in the same way as for ascending orbit, but the angle α between the true north N and the flight direction is calculated as

$$\alpha = 90° - \beta + 180°. \tag{40}$$

The viewing azimuth γ is calculated as

$$\gamma = \alpha + 90°. \tag{41}$$

Viewing azimuth was calculated for each image containing the selected point in the selected time range and was saved as image property for further computations.

Fig. 15 Calculation of the view azimuth for the ascending orbit

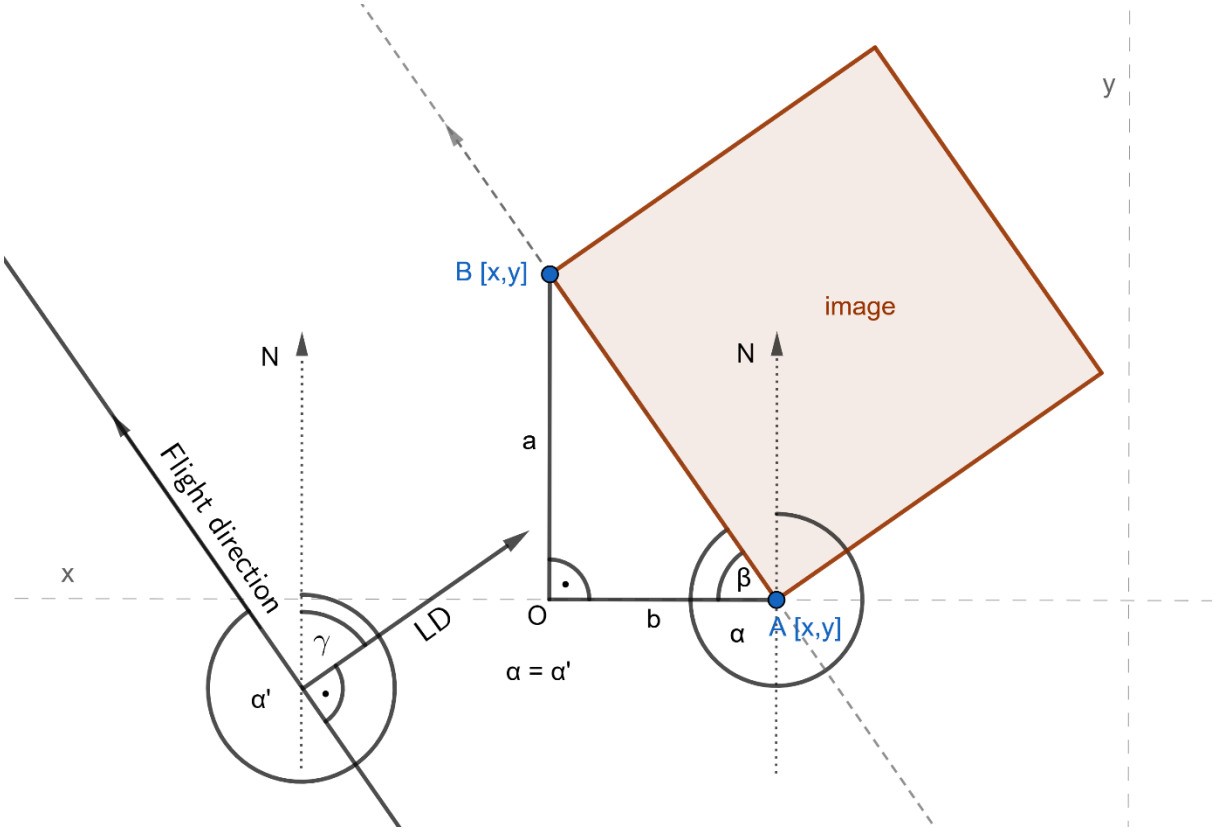

Source: own work

Fig. 16 Calculation of the view azimuth for the descending orbit

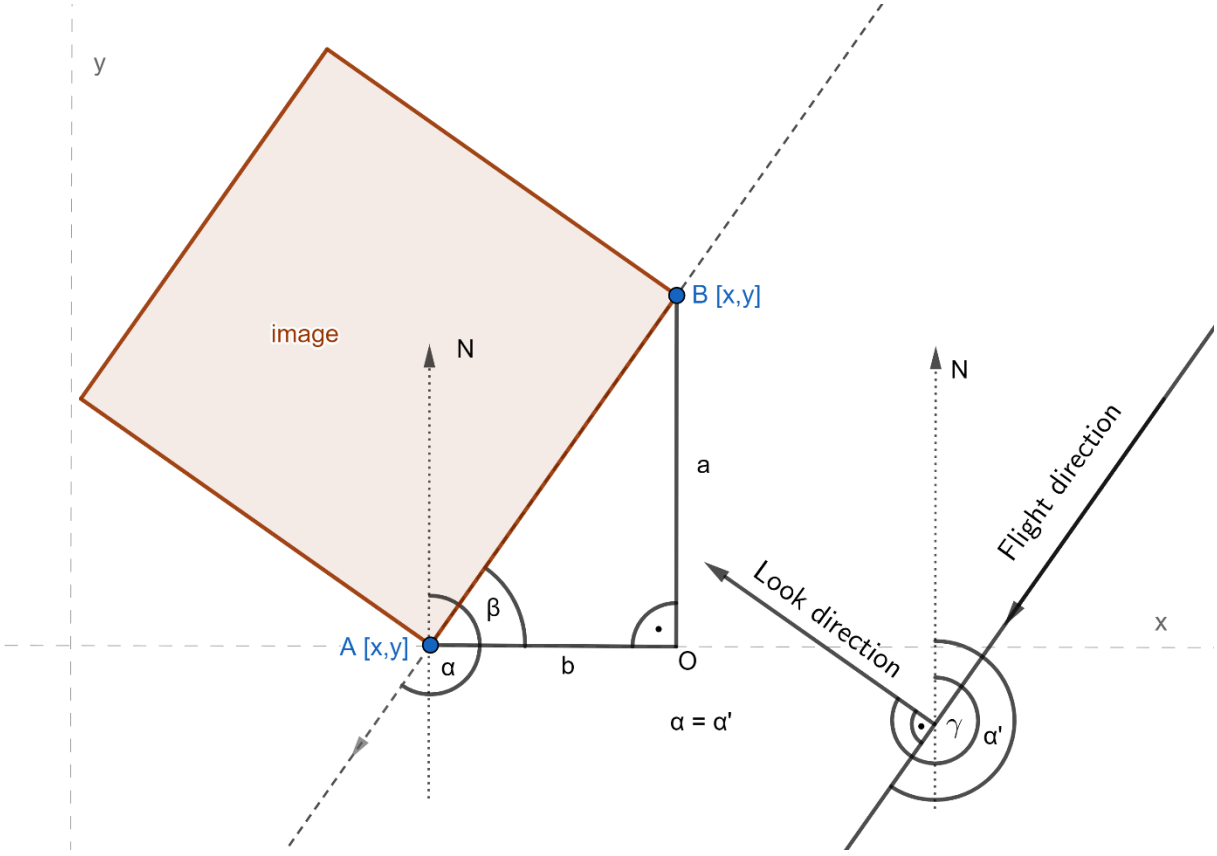

Source: own work

2.4.3 Linear relationship of backscatter and LIA

Pairman et al. (1997) suggested that the selection of data points from pure land cover class can yield to better relationship between backscatter and local incidence angle. Hinse, Gwyn, Bonn (1988) choose areas from the same land cover class for successful results in the incidence angle correction. In our analyses we also focused on one type of land cover, either deciduous or coniferous forests.

1000 random points were generated in each study area to ensure the highest possible representation of forests in the area. A 20 m buffer was created around these random points and mean values of was calculated for each input band (LIA, VV and VH backscatter) to ensure the reduction of speckle effect. The calculation of statistics (in our case mean value) from a given region (20 m buffer) in GEE was done using a weighted reducer method, where „pixels are included if at least (approximately) 0.5% of

the pixel is in the region“ and „their weight is the minimum of the image's mask and the (approximate) fraction of the pixel covered by the region“ (GEE 2020a). At the same time, a forest mask was generated from the combination of CLC2018 and Hansen et al.’s Global Forest databases. In our study, the base layer from 2000 of Hansen et al.’s Global Forest database was used where only forest pixels with >50% crown cover were selected. After that, pixels corresponding to the forest loss from 2000 till 2018 were masked out from the base layer. The resulted layer was overlaid with a selected forest class of CORINE CLC which resulted in a final forest mask. For further analysis, buffered random points (created from 1000 random points) lying completely inside the forest mask were selected (hereafter referred to as “forest areas”), ensuring that only forest areas will serve as input data to the regression analysis. These forest areas were overlaid with Sentinel-1 images and the and mean values of backscatter and LIA values were extracted. As these areas are represented by a circle with 20 m radius, this should ensure the reduction of speckle effect. Using these areas, a scatterplot was created, and the least squares estimate of a linear function of one variable with a constant term was calculated by

$$\sigma_{pred} = a + b * \theta_0 \tag{42}$$

where σ_{pred} represents the estimated value of the backscatter σ_0, θ_0 is LIA, a and b are offset and slope of the regression line, respectively.

The generation of forest areas and the subsequent calculation of offset and slope values of the linear regression line was performed for each image in the selected time and spatial range separately. These values were saved as image properties for the next computations.

2.4.4 Apply the incidence angle correction

After the calculation of the regression line parameters, the elimination of the effect of different LIAs was done by calculating a new (reference) backscatter value σ^0_{ref} for the studied area as if the local incidence angle θ_0 at each image was the same θ_{ref}, given by the equation:

$$\sigma^0_{ref} = \sigma^0_0 - b\ (\theta_0 - \theta_{ref}) \tag{43}$$

where σ_0^0 is the backscatter value at his original local incidence angle θ_0, b is the slope of the linear regression line and θ_{ref} is the reference incidence angle, to which the resulted backscatter is going to be corrected.

This is the same equation as used in the earlier mentioned studies which used the regression-based normalization approach, but with some modifications. The major modification is that in this study we used the LIA θ_0, instead of radar incidence angle θ. The next improvement was applied to the θ_{ref} in the time series analysis where only one case study (circle area with a 20 m radius) was analysed. Here, the mean value was calculated from the minimum and maximum LIA. In our selected case studies, there are three or four different overlapping satellite paths, so we can obtain three of four different values of LIA. Therefore, the minimum and maximum values do not represent extreme values, but values that are periodically appearing in a time series. The mean value is a specific value for the selected area and is aimed to achieve results without (or with less) fluctuations of backscatter value in the time series analysis, which are caused by combination of different paths and orbits resulting in different LIAs. For statistical comparison of study areas and evaluation of the proposed method, the same LIA value was used for each study area – 38.5° as a centre incidence angle of a Sentinel-1 IW GRD data swath. Also, another modification is that we used a land-cover specific approach for calculation of the backscatter-LIA dependence for each individual image separately.

2.4.5 Comparison of study areas and their accuracy assessment

To compare sets of generated forest areas within our study areas, some statistics were calculated including mean elevation of these forest areas, LIA range, LIA interquartile range (IQR). For possible comparisons and evaluation, mean values of linear regression line slope (parameter b), R^2 and p-value for both polarizations were calculated from all available images from the time range June-August 2019. The IQR was calculated as the difference between 75th (Q3) and 25th (Q1) percentiles of observed LIAs (44).

$$IQR = Q3 - Q1 \tag{44}$$

Then, an accuracy assessment was done, which was based on comparing some statistical parameters before and after the LIA correction. These parameters include backscatter range (MAX-MIN), variance and standard deviation of backscatter, as it was done in previous studies (i.e. in Bayer, Winter, Schreier 1991; Hinse, Gwyn, Bonn 1988; Topouzelis, Singha 2016; Truckenbrodt et al. 2019). Hinse, Gwyn, Bonn (1988, p. 128) stated that "a reduction of the variance indicates a reduction of the topographic effects in the corrected SAR data". Bayer, Winter, Schreier (1991) also confirmed this statement. According to them, in our study we also assume that the reduction in variance, standard deviation and range of backscatter indicate the improvement of data, thus elimination of LIA effects. For calculation of these statistical parameters, outliers were excluded in each list of backscatter values using upper and lower fences, so in analyses we used only data with backscatter values lower than the upper fence (45) and higher than the lower fence (46).

$$\text{Upper fence} = \text{Q3} + (1.5 * \text{IQR}) \tag{45}$$

$$\text{Lower fence} = \text{Q1} - (1.5 * \text{IQR}) \tag{46}$$

These statistics were extended by percentual changes after the correction:

$$\Delta S = \left[\frac{S_{corr} - S_{uncorr}}{S_{uncorr}}\right] * 100\ \% \tag{47}$$

where S represents the statistical parameter (range, variance, or standard deviation), ΔS is the percentual change after the correction, S_{uncorr} and S_{corr} are the statistical parameters before and after the correction, respectively.

In the next step, we wanted to find, whether LIA range, LIA IQR or mean elevation of the forest areas has the primary influence on the found statistical values, so correlations were calculated for relationship between these parameters and found statistical parameters.

The correlation coefficient of regression lines for corrected and uncorrected data were also compared. Short-time series were then created for four case studies and a few statistical evaluations (range, variance, standard deviation) comparing time series behaviour before and after the correction was made.

2.4.6 Comparison of the proposed method with Terrain Flattening

In the last step, we compared results using our methodology with data from desktop processing using method of Terrain Flattening (TF) developed by Small (2011). For the comparison we selected case study 1 - coniferous forest in the Low Tatras NP - with high LIA range (69°). We downloaded 58 Sentinel-1 images for a 3-month period (June-August 2019) from the Copernicus Open Access Hub. Data were pre-processed in SNAP software using the same pre-processing steps as in GEE, just the Terrain Flattening was implemented, too. The processing chain was as following: Apply Orbit File, Remove GRD Border Noise, Thermal Noise Removal, Radiometric Calibration, Radiometric Terrain Flattening, Terrain Correction, Conversion from Linear values to dB. The calculations were run on a desktop computer with a 64 GB RAM, 3.1 GHz, 14-core Intel Core i9-7940X CPU and an 8 GB GPU (with 32 GB shared GPU) using NVIDIA GeForce GTX 1070.

3 Results

3.1 Linear relationship between backscatter and LIA

To test the influence of LIA on backscatter value, forest areas generated in the study areas were used. This was done for each image separately in a short-term time series for a summertime (June - August 2019). For each study area, in average 410 forest areas were included in the regression analysis (tab. 5). Appendix 1 shows a distribution of generated forest areas classified according to their LIA in study area 1 (Sentinel-1B image from 3rd July 2019, from descending orbit no. 51 was used). Statistics were calculated for forest areas (mean elevation, LIA range, LIA interquartile range (IQR)) and for possible comparisons and evaluation, mean values of linear regression line slope (parameter *b*), R^2 and p-value for both polarizations were calculated from all available images from the selected time range (tab. 5). For these study areas we created boxplot graphs representing the distribution of LIA for forest areas where differences in IQR are also visible (fig. 17).

The negative linear relationship between the backscatter of forest areas and LIA was proven in each study area, where the backscatter is decreasing with the increasing LIA. This negative linear behaviour proves the effect of the terrain and reinforces the importance of their elimination.

Fig. 17 Boxplots of LIA for forest areas in each study area

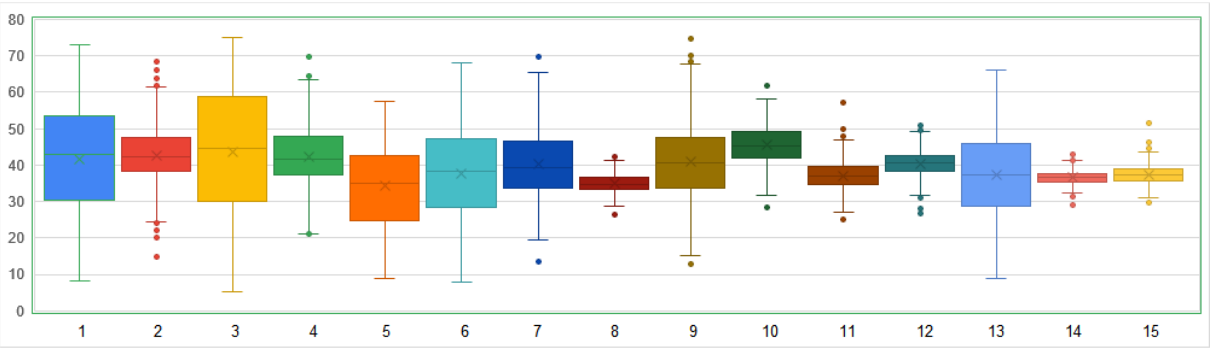

Source: own work

Tab. 5 Statistics of selected study areas for all the available Sentinel-1 imagery in the summer period (June-August 2019). Areas marked with * are broadleaf forests.

Study area	Scale VH	Scale VV	R2 VH	R2 VV	p-value VH	p-value VV	Elevation (m)	LIA range	IQR	Number of forest areas
1	-0.205	-0.214	0.70	0.72	5.1E-76	2.1E-88	1087	64.72	23.11	360
2	-0.182	-0.182	0.46	0.49	3.9E-39	7.0E-44	974	53.80	9.30	347
3	-0.221	-0.229	0.75	0.76	4.9E-87	3.3E-85	1120	69.67	28.80	314
4	-0.168	-0.170	0.40	0.43	5.5E-27	2.5E-33	1007	48.52	10.70	320
5*	-0.168	-0.177	0.59	0.64	1.5E-40	1.0E-53	311	48.49	17.65	545
6*	-0.176	-0.182	0.65	0.69	1.8E-120	6.8E-134	782	59.81	18.93	600
7*	-0.150	-0.153	0.43	0.46	1.1E-48	5.8E-50	448	56.21	12.91	506
8*	-0.093	-0.115	0.03	0.06	0.089	0.035	154	15.86	4.49	152
9*	-0.165	-0.176	0.56	0.60	4.9E-71	4.2E-77	372	61.68	13.66	430
10	-0.138	-0.147	0.16	0.19	2.0E-11	4.1E-14	659	33.37	7.17	449
11	-0.146	-0.150	0.16	0.18	1.1E-12	1.2E-14	704	31.89	5.19	472
12	-0.103	-0.107	0.06	0.07	0.002	0.002	517	25.28	4.45	421
13	-0.177	-0.186	0.54	0.57	1.3E-85	3.2E-95	733	57.19	17.10	548
14	-0.145	-0.134	0.04	0.04	0.002	0.004	218	14.72	2.33	362
15	-0.129	-0.123	0.06	0.06	0.005	0.005	170	21.67	3.34	321

Source: own work

Several significant findings were found from the statistical analysis (see tab. 5):

1. Dependence of backscatter on LIA was in almost every case statistically highly significant at the significance level of 0.1 % (p-value < 0.001), while study areas 12, 14 and 15 was very significant at significance level of 1 % (p-value < 0.01). In case of study area 8 for VV polarization, the correlation is statistically significant for the significance level of 5 %. For VH polarization of the study area 8 the mean p-value is higher than 0.05, which indicates very weak or no correlation at all. However, when analysing single images, the maximum p-value achieved in study area 8 was 0.55 for both polarizations and for study area 15 it was around 0.2 for both polarizations. This means that in some cases we can not reject the null hypothesis: that there is no correlation between the LIA and backscatter (correlation = 0). So, in these cases, the correlation is very weak, or no correlation exists at all.

2. The highest linear regression slope values (higher than 0.2 db/degree for both polarizations) were achieved in areas, where forest areas had the mean LIA higher than 64°. The lowest regression slope value was achieved in study areas 12 and 8 (around 0.1 db/degree for both polarizations).

3. The coefficient of determination R^2 is slightly higher for the VV polarization in each case. Also, the p-value is lower for VV polarization than for VH (except for study

areas 14 and 15) - so the statistical significance of the correlation between LIA and backscatter is slightly higher for VV polarization. Also, the slope of the regression line is steeper (higher) almost for each case in VV polarization, compared to VH (except of study areas 2, 14 and 15).

In the next step, we were assuming that the LIA range has the biggest influence on the other statistics, so the correlation between LIA range for each study area and other statistics from tab. 2 (R^2, elevation, p-value and linear regression line slope) were evaluated. A strong and statistical significant correlation (R^2 = 0.89, p-value = 1.1E-07) was found in the linear relationship between LIA range and coefficient of determination R^2, while weak but also statistical significant (at significance level of 1 %) was found between LIA range and linear regression line slope values and elevation, respectively. According to these comparisons from tab. 6, the biggest influence on R^2 has the LIA range. Mean elevation of the selected forest areas had weaker influence on the R^2 or slope values, but they are still statistically significant at significance level of 5 %. At all, the higher the mean elevation, the wider is the LIA range, which was statistically also been proven. The p-value is weakly correlating with LIA range and elevation and number of forest areas in the selected area had no effect on the R^2 nor p-value.

Tab. 6 Statistical evaluation of linear dependency between obtained LIA range, elevation, slope values, R^2 and p-values for study areas (from tab. 5) for VV polarization

	R2	p-value
LIA range vs R2	0.89	1.10E-07
LIA range vs elevation	0.45	0.006
LIA range vs slope	0.51	0.003
Elevation vs slope	0.28	0.042
Elevation vs R2	0.33	0.025
Elevation vs p-value	0.28	0.041
LIA range vs p-value	0.23	0.069

Source: own work

3.2 Correction of LIA

Based on the scatterplots (fig. 18), it can be clearly seen, that the correction was processed. To measure the effectivity/accuracy of the correction, we conducted some statistical tests on the selected forest areas for each study area for the first image in the collection from time 1st of July. We excluded the extreme values using lower and upper fence (as used in boxplots). Using these data without extreme values we compared the range of the backscatter (max - min), variation of data and standard deviation for VV and VH polarizations before and after the correction.

Fig. 18 Comparison of relationships between VH and LIA for forest areas in the surrounding of the study area 1 before and after the correction

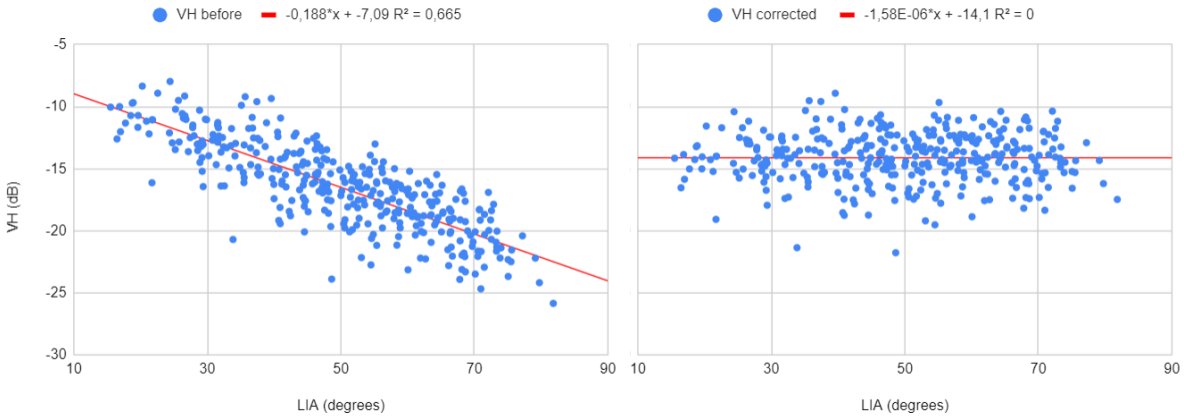

Source: own work

We assume that eliminating the backscatter-LIA dependence (improvement in results) will result in a reduction in the range of backscatter, variance, and standard deviation after LIA correction using our method. Results (fig. 19) show a clear decrease of variance, standard deviation, and range of backscatter values for both polarizations. These statistical comparisons showed a decrease of variance and standard deviation for each study area in both polarizations. In the range of backscatter values the decrease after correction was noticed almost in all cases, except for study area 8 (both polarizations) and for study area 11 (VH polarization), where in contrast, an increase of backscatter range was observed (fig. 19). For study areas where higher than 17° LIA IQR were found (fig. 17) (study areas 1, 3, 5, 6 and 13), the difference between the original and corrected values for mentioned statistical parameters was significantly higher compared to other localities. Reduction of the range by more than 50 % was

made for both polarizations for study areas 3 and 6, while a reduction by more than 35 % was made for study areas 1, 5 and 13. The lowest reduction of backscatter range (by less than 10 %) was made to study areas 8, 11, 12, 14 and 15 which LIA ranges were less than 32° and interquartile range was less than 5°.

The highest variance in non-corrected data was found in study areas, which had range of LIAs higher than 64° with LIA IQR > 23° - 13.6 dB for both polarizations for study area 1, and higher than 17 dB for both polarizations for study area 3. Study areas with higher LIA range showed the highest improvement in variance after correction in means up to 16.5 dB in case of study area 3, which represents improvements by more than 80 %. Improvement in both polarizations by more than 50 % was achieved also in study areas where forest areas had LIA range higher than 50° with LIA IQR > 10° (study areas 4, 5, 6, 9 and 13). However, high variance in the data with high LIA range and LIA IQR (study areas 1 and 3) remained also after the correction (in average 3.3 dB and 3.5 dB for VV and VH polarization, respectively) compared to other data (in average 1.9 dB and 2.4 dB). For study areas where forest areas achieved LIA range lower than 35° with LIA IQR > 7°, the variance was reduced by less than 25%.
The standard deviation comparison showed a similar behaviour as the variance.

Fig. 19 Statistics of selected forest areas within each study area from the linear regression analysis before and after the LIA correction

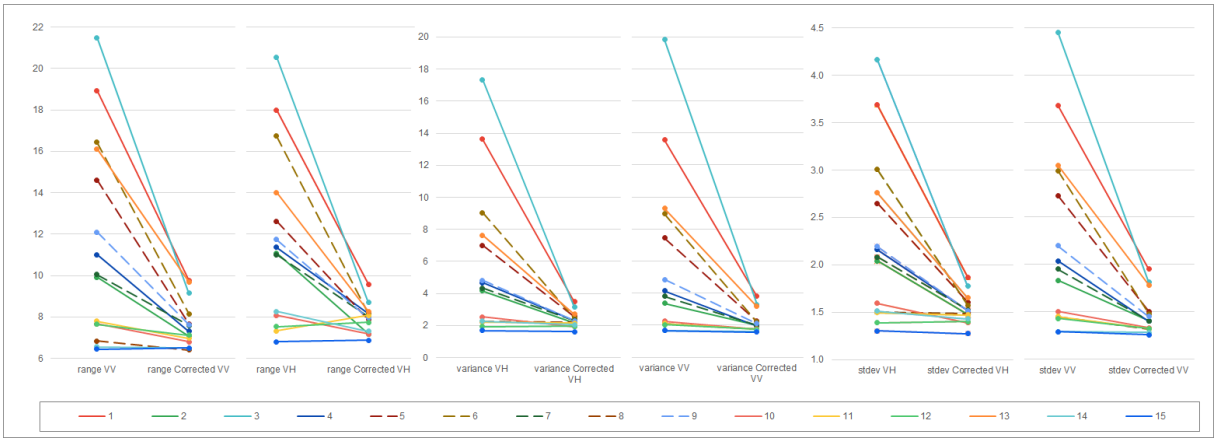

Source: own work. Explanatory notes: Study areas with dashed lines represent broadleaf forests.

3.3 Time series analysis

The time series graph in fig. 20 shows a comparison of the original backscatter values in VV and VH polarization and LIA values for case study 1 with LIA range 69°. It can be clearly seen that the backscatter values are influenced by LIA – periodic fluctuation of LIA causing a periodic fluctuation of backscatter values. It is evident, that with increasing LIA, the backscatter is decreasing and vice versa.

Fig. 20 Comparison of backscatter and LIA values for case study 1

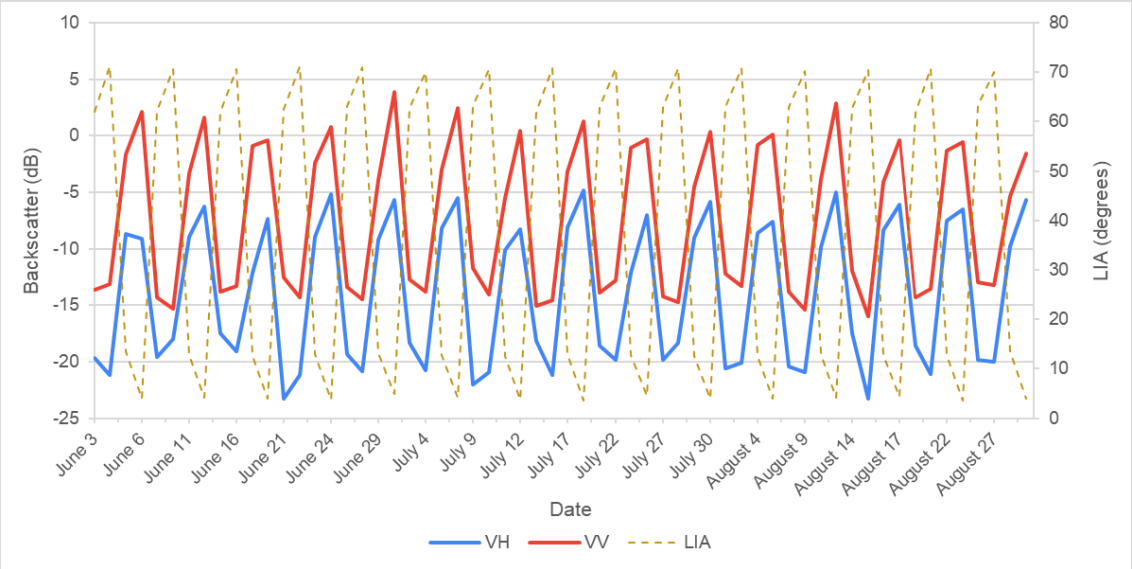

Source: own work

Fig. 21 represents short-term time series for four case studies with different LIA ranges. In the short-term time series analysis (June-August 2019), all available data from each path, orbit and satellite were evaluated. In the original non-corrected time-series the fluctuation of backscatter values influenced by LIA can be seen, mainly in case study 1 (fig. 21 a) and 2 (fig 21 b), while after the correction, the time series become smoother. According to fig. 20 we assume that different LIAs on different acquisition paths for the studied area cause variation (fluctuation) of data through the time. After the correction of LIA effects using our method, the resulted time series are obviously smoother compared to uncorrected, thus when the variance and standard deviation is lower, the accuracy of the model will be higher. For purpose of an assessment of our method, we compared variance, backscatter range and standard deviation of the short-term time series before and after the correction. Results in tab. 5 show decrease of these statistical parameters after the correction. For case study 1 with

the highest LIA range (69°), correction made a reduction of variance by 95 %, and reduction was significant (by more than 70% in both polarizations) also for backscatter range and standard deviation. For case study 4 it was a >75% reduction of variance and >40% of standard deviation. For case study 6, the variance was reduced by less than 55%, standard deviation by less than 35%. For case study 12 with lowest LIA range (with a 13° LIA range using 3 different paths), the variance was reduced by only 13 % for VH and 6 % for VV polarization.

Fig. 21 Short-term time series analysis of corrected and uncorrected data for selected case studies with different LIA ranges

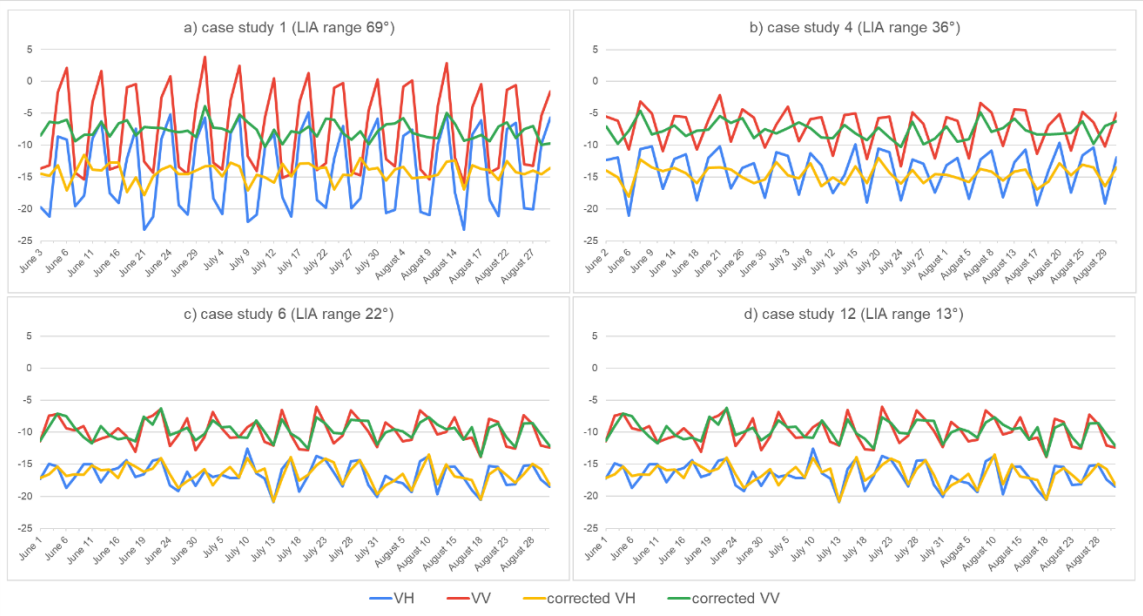

Source: own work

From the fig. 21 and statistics in tab. 7 it is apparent that after the elimination of terrain effects using the proposed land-cover specific regression-based correction of LIA, time series become smoother mainly in case studies with wide range of LIAs (fig. 21 a). In case of low LIA range, the effect of correction is only marginal (fig. 21 d). For LIA ranges higher than 20°, the effect of correction is more apparent, and this demonstration also proves, that the correction is more suitable for case studies with wider range of LIA. Another finding in time series graphs was, that in each cases the backscatter in VV polarization was higher by about 6-7 dB than in VH.

Tab. 7 Statistics of corrected and uncorrected data in the short-term time series

	Case study 1			Case study 4			Case study 6			Case study 12		
	Var.	range	Stdev	Var.	range	Stdev	Var.	range	Stdev	Var.	range	Stdev
Original VH	43,63	18,42	6,61	9,39	10,89	3,07	4,59	9,29	2,14	1,59	4,85	1,26
Corrected VH	1,88	5,27	1,37	2,29	6,77	1,51	2,71	8,23	1,65	1,39	4,57	1,18
Original VV	46,47	18,87	6,82	9,76	9,65	3,12	4,20	8,35	2,05	1,95	7,74	1,40
Corrected VV	2,28	5,24	1,51	2,09	6,55	1,45	1,98	6,78	1,41	1,84	6,91	1,36

Source: own work

3.4 Comparison of our method with desktop-based method of TF

In the last part of this work, we compared the accuracy of our proposed method with the desktop-based method of TF over case study 1. In the fig. 22 it can be clearly seen that in the time series for data corrected using TF (TF VH or TF VV), the fluctuation of data remained higher compared to data obtained from our proposed method (corrected VV or corrected VH). After data pre-processing in SNAP we obtained NoData values for some dates for the selected case study. It happened too, that for VV polarization we got data, while for VH not. For now, we do not have an explanation for that. After the comparison of variance in backscatter we found that the variance in data corrected using the TF is much higher (7 dB and 8 dB for VV and VH variance, respectively) than in data using our proposed method (1.8 dB for both polarizations) (tab. 8). It means a reduction of variance by about 75 % for both polarizations using our proposed method compared to TF.

When taking into consideration the pre-processing time of the images in the desktop environment with a computational power mentioned in section 2.4.6, for TF method it took about 19 minutes for one image. As in GEE the Sentinel-1 images are already pre-processed and to correct data using the proposed terrain correction method takes only a few seconds for a three-months period.

Tab. 8 Comparison of variance in both polarizations using TF and our proposed method

	TF	Corrected	Percentual change
variance VV	7.09	1.80	75%
variance VH	8.41	1.85	78%

Source: own work

Fig. 22 Comparison of TF and our method for short-term time series for case study 1

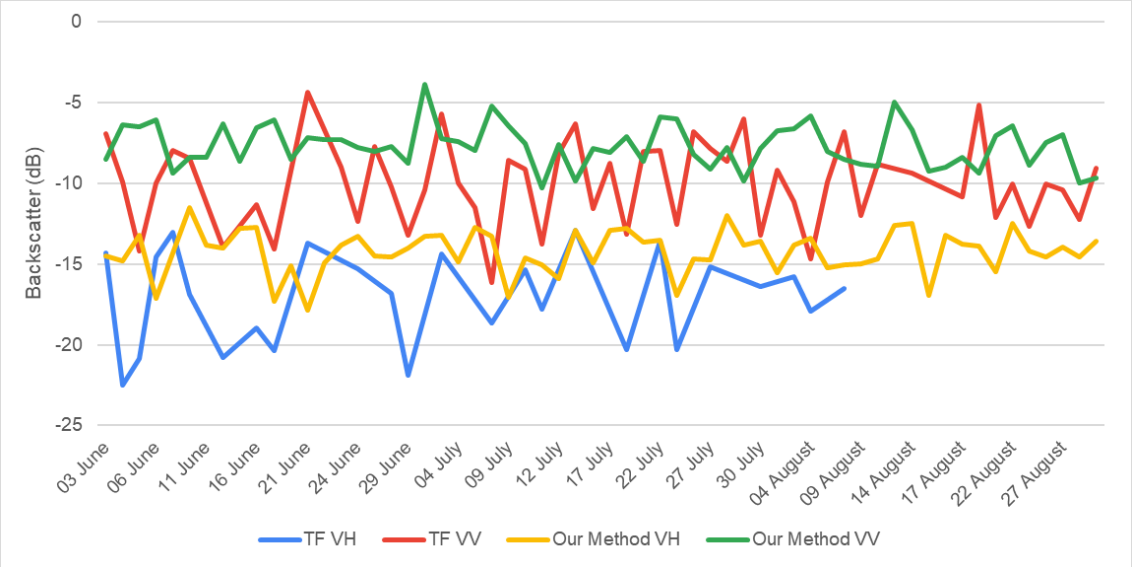

Source: own work

4 Discussion

Remote sensing in the microwave electromagnetic spectrum has many advantages compared to optical data, like daylight and weather-independent sensing. Since the launch of Sentinel-1 in 2014 with freely available SAR data, new opportunities in forest monitoring have been opened to a wider research community. However, the interaction between the SAR signal and the surface is different from the optical signal's interaction. Tilted terrain can have a strong influence on the resulted backscatter. This influence is most pronounced at higher altitudes when combining images from different orbits and paths to create a time series analysis (fig. 20). It needs to be corrected before any further analysis over areas with mountainous terrain.

In this study, we developed and tested a method that aims to eliminate the effects of terrain on backscatter values over forested areas. This method is mainly intended for use in time series analysis, where images with different imaging geometry are combined. The traditional method for achieving comparable images is based on using images with the same imaging geometry – from the exactly same path, orbit and satellite (i.e. in Kaasalainen et al. 2010 and Rauste et al. 2016). However, a drawback in case of using only data from the same orbital plane leads to a worse temporal resolution. Taking into consideration all the images over a given area can dramatically increase the temporal resolution. Especially in the case of Sentinel-1 mission which is composed of a constellation of two satellites sharing the same orbital plane. In our case for most of the areas, four different paths were available for a given study site. It resulted in 60 images available in a three months period instead of 15.

If using images from several paths, it is necessary to take into consideration that (local) incidence angles will be different for a study area. Especially, in mountainous regions, effects of terrain can largely influence the backscatter over the studied area. With the calculation of local incidence angle (LIA), we can obtain a value which involves effects of topography (slope and aspect), radar look angle and radar incidence angle.

In this study, the relevance of the proposed LIA correction method using C-band SAR data was proven in several case studies from different parts of Central Europe. In this method, regression line coefficients were calculated separately for each image from selected forest areas located in a study area. As the land-cover specific backscatter-LIA dependence is calculated for each image separately, the effect of different seasons

(seasonality in data) through the year has low influence on the results. This method is different from the traditional pixel-based method used in previous studies (Nguyen et al. 2015; Dostálová et al. 2016; Pathe et al. 2009 and others), where the regression coefficients were derived for each pixel separately using all the available images from a selected time period.

An essential decision before processing a huge amount of data (tens or hundreds of SAR images for a 3-months or 5-year period, respectively per case study) is to choose a suitable software and hardware for that purpose. In this work we used and tested a cloud-based solution GEE, where all the data and processing power is stored. GEE is probably the most used and the most well-known cloud-based platform in the remote sensing community.

Results showed an obvious negative linear relationship between backscatter and LIA, similarly as in other studies (e.g. in Truckenbrodt et al., 2019). That relationship is caused mainly by slope and aspect of the terrain with respect to the incoming radar signal. Our method is eliminating this effect. However, this linear relationship can be biased by some outliers (backscatter values) that may represent non-forest areas included in the regression due to errors in the land cover databases used. Our approach based on the combination of two land cover databases should reduce the possibility of these errors. Outliers in the regression analysis can represent forests with different density of trees, but by selecting only pixels with at least 50 % of tree canopy coverage (from the Hansen database) we tried to reduce these errors.

Statistical analysis of forest areas in 15 selected study areas showed that the dependence of LIA on backscatter is increasing with the increasing LIA range and LIA IQR. For the study areas, where only a low range of LIA and LIA IQR was found (like in study areas 8 and 15), for some dates the correlation between backscatter and LIA was very weak or no correlation existed at all. An interesting finding is that the R^2 is slightly higher, the slope of the regression line is steeper (bigger change in backscatter is caused by LIA), and the p-value is lower in most of the cases for the VV polarization compared to VH. For that finding we haven't found an explanation yet.

Compared to earlier studies based on C-band data (i.e. Mougin et al. 1995 or Frison, Mougin 1996), where a flat angular behaviour was detected over forests (regression line slope a = 0.06), or where only a weak correlation with a slight negative slope was experienced (Hinse, Gwyn, Bonn 1988), in this study a relatively strong correlation with steep slope values were found. Linear regression line slope was higher

than 0.2 db/degree for study areas with LIA range higher (of forest points) than 64° and LIA IQR > 23°. The lowest regression slope value was achieved in study areas 8 and 12 (around 0.1 db/degree), which had LIA range 25°. Strong and statistically significant correlation was found between LIA range and R^2.

Statistical comparisons of uncorrected and corrected forest areas involved in the regression analysis showed reduction in terms of backscatter variance and standard deviation after correction in all study area. The biggest improvement in variance - higher than 50% reduction - was found in study areas, where the LIA range of forest areas was higher than 50° and IQR > 10°. When compared to earlier studies, Hinse, Gwyn, Bonn (1988) applied a cosine square correction and reduced a maximum of 10 percent of variance caused by incidence angle. Bayer, Winter, Schreier (1991) reduced the variance for forested areas by 5-13 %. In our case, these range of reductions appeared in study areas with LIA range lower than 25° and IQR > 4°. However, the variance in data sets remained higher (around 3.5 dB) for LIA ranges higher than 64°, while for other data sets it was around 2 dB. High variance of backscatter in the forest areas after the correction can be caused by generally high heterogeneity of forest vegetation (different types of trees, different growth stage or density of trees involved in the regression analysis), which is especially higher with higher altitudes, as was also mentioned in Pairman, Belliss, Mcneill (1997).

The validation of effectivity of the proposed correction method applied in a short-term time series analysis using all available Sentinel-1 paths showed that the LIA correction is the most effective in case studies where a big range of LIAs can be found for the case study. For case studies where range of LIA was lower than 20° the correction was almost not apparent at all. These results are similar the results in Hinse, Gwyn, Bonn (1988), where for pixels at local incidence angle less than 26° did not occurred any significant correction using semi-empirical cosine-based methods. They also found that pixels with higher slope angles have stronger correlation to the backscatter value. However, after the correction, some fluctuation of values in the time series remained, which can be attributed to random short-term variations caused by environmental factors, like increased moisture or different reflectivity of the forest caused by different sensing time (5 A.M. vs 4 P.M). This different reflectivity can be caused by for instance by change of temperature between these two times, change in moisture, different nature of the leaves, etc. According to influence of precipitation, Frison et al. (2018) did not find any relationship between precipitation and backscatter

values over forested areas using Sentinel-1 data. They explained this behaviour by the difference between the measured precipitation and the precipitation that can be retained by the leaves or needles of a tree. Tanase et al. (2019) also found that C-band was less sensitive to vegetation water content (variations about 1 dB) compared to P- and L-band. Remained fluctuation can also be caused by speckle noise which was not sufficiently removed by a 20 m buffer area.

Higher obtained backscatter in VV polarization compared to VH over forested areas can be explained by higher attenuation of VV polarization by vegetation cover compared to VH, as it was found also in Yunjin Kim, van Zyl (2002). This results is similar to previous studies over forested areas (i.e. Dostálová et al. 2018; 2016; Frison et al. 2018).

According to the comparison with desktop-based method using TF, our method showed improvement of the results in terms of lower fluctuation of backscatter values in the time series analysis and of reduced variance by about 75 % for an case study 1 with LIA range 69°. According to our results, the computational time of these two methods are incomparable. The pre-processing of Sentinel-1 data to correct the terrain effects for a three-month long period in SNAP took several hours compared to GEE, where it was a few seconds.

Our LIA correction method was implemented to the GEE and is available as a freely available function using the requirement call:
require('users/danielp/LIA_Correction:LIA_Correction_Function').
The full code with the explanation of input parameters and an example code of usage was added as an electronic attachment to this work, described in the Attachment 2.

5 Conclusion

In our study we developed a land cover specific LIA correction method for SAR data. It was tested in the selected protected areas in Central Europe, followed by an evaluation of its relevance and accuracy. For this study, we used open-access data Sentinel-1, SRTM DEM, CORINE CLC, Hansen Global Forest Database and, for research purposes, freely available cloud-based platform GEE. Based on our achieved results and their statistical evaluation, data after LIA correction showed reduction of statistical parameters (range, variance, and standard deviation), which means reduction or terrain-induced effects on backscatter values. This reduction was greater in areas with big difference in LIAs obtained from different paths. In the short-term time series, data after correction showed smoother behaviour (without significant fluctuation caused by different LIA) compared to uncorrected data, where the reduction of variance was by up to 95 %. In comparison with the most used terrain correction method of TF (developed by Small, 2011) in the desktop environment, our proposed method showed lower fluctuation of backscatter values in the subsequent acquisitions and lower variance in a three-month long time series. Moreover, processing time of these two methods are incomparable. GEE is based on cloud platform and stores already pre-processed Sentinel-1 SAR data. The pre-processing using our LIA correction method took a few seconds, while the pre-processing of a single image in a desktop-based environment took about 19 minutes (using the higher-mentioned computation power of the PC). This comparison also highlights the efficiency of the cloud-based methods in analysing big amounts of satellite data (big data). As an important output of this work, we have prepared a freely available GEE algorithm which applies our developed method to the selected collection of Sentinel-1 images (see Appendix 2, available also at https://code.earthengine.google.com/d1e71db16a0a8861269469b0b914a2d8).

The main limitation of this study is that the methodology is focused only on forests. In the following studies it would be appropriate to test and statistically evaluate the results in areas with different types of vegetation, as well as in areas without vegetation. Another limitation of this study is that the methodology was tested in the countries of the European Union, for which is the CORINE CLC dataset available. In the case of application of this method in other countries out of EU, it is possible to use other global, regional, or national land cover databases.

Although, there is an increasing number of studies using SAR data in the time series analyses, there are still several unanswered questions. In the next work it will be important to explain the reason of the short-term fluctuations of backscatter values in the subsequent dates. Also to try implement this methodology for long-term time series to detect seasonality or changes in forests, as well as to understand the character of the seasonal activity or in detail to access a relationship between the time series curve and characteristics of the studied area (terrain slope, aspect, elevation, LIA range or characteristics of the vegetation). In the case of long-term time series analysis, it would be appropriate to try to implement different types of change detection algorithm into GEE.

From point of view of long-term time series analysis, it should be helpful to implement radar indicators (e.g. radar polarimetric indices) to monitor the condition of forests and compare them with proven vegetation indices (NDVI, NDMI) from optical data or test the impact of precipitation on the evaluation of long-term time series and propose methods for their correction in C-band SAR data. On the other hand, the planned radar missions Biomass with P-band (2021), NISAR with L- and S-band (2022), TanDEM-L with the L-band (2022) can bring new opportunities for forest exploration and thus new challenges in data processing and analysis. ESA and NASA are jointly developing the Multi-Mission Algorithm and Analysis Platform (MAAP) cloud platform (start in 2021), which will contain and process data, mainly from Biomass, GEDI and NISAR missions.

6 References

AHERN, F. J., LECKIE, D. J., DRIEMAN, J. A. (1993): Seasonal Changes in Relative C-Band Backscatter of Northern Forest Cover Types. IEEE Transactions on Geoscience and Remote Sensing, 3, 31, 668–680.
BAYER, T., WINTER, R., SCHREIER, G. (1991): Terrain influences in SAR backscatter and attempts to their correction. IEEE Transactions on Geoscience and Remote Sensing, 3, 29, 451–462.
BOUSBIH, S., ZRIBI, M., LILI-CHABAANE, Z., BAGHDADI, N., EL HAJJ, M., GAO, Q., MOUGENOT, B. (2017): Potential of sentinel-1 radar data for the assessment of soil and cereal cover parameters. Sensors (Switzerland), 11, 17.
BOUVET, A., LE TOAN, T. (2011): Use of ENVISAT/ASAR wide-swath data for timely rice fields mapping in the Mekong River Delta. Remote Sensing of Environment, 4, 115, 1090–1101.
BÜTTNER, G., KOSZTRA, B., SOUKUP, T., SOUSA, A., LANGANKE, T. (2017): CLC2018 Technical Guidelines.
CASTEL, T., BEAUDOIN, A., STACH, N., STUSSI, N., LE TOAN, T., DURAND, P. (2001): Sensitivity of space-borne SAR data to forest parameters over sloping terrain. Theory and experiment. International Journal of Remote Sensing, 12, 22, 2351–2376.
CHAUHAN, N. S., LANG, R. H., RANSON, K. J. (1991): Radar Modeling Of A Boreal Forest. IEEE Transactions on Geoscience and Remote Sensing, 4, 29, 627–638.
DOBSON, M. C., ULABY, F. T., LE TOAN, T., BEAUDOIN, A., KASISCHKE, E. S., CHRISTENSEN, N. (1992): Dependence of Radar Backscatter on Coniferous Forest Biomass. 30, 412–415.
DOSTÁLOVÁ, A., MILENKOVIĆ, M., HOLLAUS, M., WAGNER, W. (2016): Influence of forest structure on the Sentinel-1 backscatter variation-analysis with full-waveform lidar data. European Space Agency, (Special Publication) ESA SP, February 2018, SP-740.
DOSTÁLOVÁ, A., WAGNER, W., MILENKOVIĆ, M., HOLLAUS, M. (2018): Annual seasonality in Sentinel-1 signal for forest mapping and forest type classification. International Journal of Remote Sensing, 21, 39, 7738–7760.
DURDEN, S. L., KLEIN, J. D., ZEBKER, H. A. (1991): Polarimetric radar measurements of a forested area near Mt. Shasta. IEEE Transactions on Geoscience and Remote Sensing, 3, 29, 444–450.
ESA (2020): Sentinel-1 Observation Scenario, https://sentinel.esa.int/web/sentinel/missions/sentinel-1/observation-scenario.
FARR, T. G., ROSEN, P. A., CARO, E., CRIPPEN, R., DUREN, R., HENSLEY, S., KOBRICK, M., PALLER, M., RODRIGUEZ, E., ROTH, L., SEAL, D., SHAFFER, S., SHIMADA, J., UMLAND, J., WERNER, M., OSKIN, M., BURBANK, D., ALSDORF, D. (2007): The Shuttle Radar Topography Mission. Reviews of Geophysics, 2, 45, RG2004.
FLORES-ANDERSON, A. I., HERNDON, K. E., THAPA, R. B., CHERRINGTON, E. (2019): The SAR Handbook: Comprehensive Methodologies for Forest Monitoring and Biomass Estimation. SERVIR Global Science Coordination Ofce National Space Science and Technology Center, Huntsville, AL, United States.
FOODY, G. M. (1986): An Assessment of the Topographic Effects on Sar Image Tone. Canadian Journal of Remote Sensing, 2, 12, 124–131.
FORKUOR, G., CONRAD, C., THIEL, M., ULLMANN, T., ZOUNGRANA, E. (2014): Integration of optical and synthetic aperture radar imagery for improving crop

mapping in northwestern Benin, West Africa. Remote Sensing, 7, 6, 6472–6499.
FRANKLIN, S. E., LAVIGNE, M. B., HUNT, E. R., WILSON, B. A., PEDDLE, D. R., MCDERMID, G. J., GILES, P. T. (1995): Topographic dependence of synthetic aperture radar imagery. Computers and Geosciences, 4, 21, 521–532.
FREEMAN, A. (1992): Sar Calibration: An Overview. IEEE Transactions on Geoscience and Remote Sensing, 6, 30, 1107–1121.
FRISON, P.-L., MOUGIN, E. (1996): Use of ERS-1 wind scatterometer data over land surfaces. IEEE Transactions on Geoscience and Remote Sensing, 2, 34, 550–560.
Frison, P. L., Fruneau, B., Kmiha, S., Soudani, K., Dufrêne, E., Le Toan, T., Koleck, T., Villard, L., Mougin, E., Rudant, J. P. (2018): Potential of Sentinel-1 data for monitoring temperate mixed forest phenology. Remote Sensing, 12, 10.
GAUTHIER, Y., BERNIER, M., FORTIN, J. P. (1998): Aspect and incidence angle sensitivity in ers-1 sar data. International Journal of Remote Sensing, 10, 19, 2001–2006.
GEE (2020a): Pixels in the region - Statistics of an Image Region, https://developers.google.com/earth-engine/reducers_reduce_region#pixels-in-the-region (7. 8. 2020).
GEE (2020b): Sentinel-1 Algorithms, https://developers.google.com/earth-engine/sentinel1 (15. 5. 2020).
GEE (no date): SRTM Digital Elevation Data 30m, https://developers.google.com/earth-engine/datasets/catalog/USGS_SRTMGL1_003#description (14. 5. 2020).
GORELICK, N., HANCHER, M., DIXON, M., ILYUSHCHENKO, S., THAU, D., MOORE, R. (2017): Google Earth Engine: Planetary-scale geospatial analysis for everyone. Remote Sensing of Environment, 202, 18–27.
GUCCIONE, P., LOMBARDI, A., GIORDANO, R. (2016): Assessment of seasonal variations of radar backscattering coefficient using sentinel-1 data. International Geoscience and Remote Sensing Symposium (IGARSS), 2016-Novem, 3402–3405.
HAMUNYELA, E., VERBESSELT, J., BRUIN, S. De, HEROLD, M. (2016): Monitoring Deforestation at Sub-Annual Scales as Extreme Events in Landsat Data Cubes.
HANSEN, M. C., POTAPOV, P. V., MOORE, R., HANCHER, M., TURUBANOVA, S. A., TYUKAVINA, A., THAU, D., STEHMAN, S. V., GOETZ, S. J., LOVELAND, T. R., KOMMAREDDY, A., EGOROV, A., CHINI, L., JUSTICE, C. O., TOWNSHEND, J. R. G. (2013a): High-Resolution Global Maps of 21st-Century Forest Cover Change. Science, 6160, 342, 850–853.
HANSEN, M. C., POTAPOV, P. V., MOORE, R., HANCHER, M., TURUBANOVA, S. A., TYUKAVINA, A., THAU, D., STEHMAN, S. V., GOETZ, S. J., LOVELAND, T. R., KOMMAREDDY, A., EGOROV, A., CHINI, L., JUSTICE, C. O., TOWNSHEND, J. R. G. (2013b): Supplementary materials for High-Resolution Global Maps of 21st-Century Forest Cover Change. Science, 6160, 342, 850–853.
HANSEN, M., POTAPOV, P., MARGONO, B., STEHMAN, S., TURUBANOVA, S., TYUKAVINA, A. (2018): User Notes for Version 1.6 of Global Forest Change 2000–2018, http://earthenginepartners.appspot.com/science-2013-global-forest/download_v1.6.html (13. 5. 2020).
HINSE, M., GWYN, Q. H. J., BONN, F. (1988): Radiometric Correction of C-Band Imagery for Topographic Effects in Regions of Moderate Relief. 2, 26, 122–132.
KAASALAINEN, S., HYYPPÄ, J., KARJALAINEN, M., KROOKS, A., LYYTIK?INEN-SAARENMAA, P., HOLOPAINEN, M., JAAKKOLA, A. (2010): Comparison of terrestrial laser scanner and synthetic aperture radar data in the study of

forest defoliation. International Archives of the Photogrammetry, Remote Sensing and Spatial Information Sciences - ISPRS Archives, January, 38.
KIM, Y., VAN ZYL, J. (2000): On the relationship between polarimetric parameters. In: IGARSS 2000. IEEE 2000 International Geoscience and Remote Sensing Symposium. Taking the Pulse of the Planet: The Role of Remote Sensing in Managing the Environment. Proceedings (Cat. No.00CH37120). IEEE, 1298–1300.
KOLÁŘ, J. (2008): Radarová data a jejich využití. Czech Space Office, Prague.
KOSZTRA, B., BÜTTNER, G., HAZEU, G., ARNOLD, S. (2019): Updated CLC illustrated nomenclature guidelines.
LASTOVICKA, J., SVEC, P., PALUBA, D., KOBLIUK, N., SVOBODA, J., HLADKY, R., STYCH, P. (2020): Sentinel-2 Data in an Evaluation of the Impact of the Disturbances on Forest Vegetation. Remote Sensing, 12, 12, 1914.
LE TOAN, T. (2007): Introduction to SAR Remote Sensing, Advanced Training Course on Land Remote Sensing, https://earth.esa.int/landtraining07/D1LA1-LeToan.pdf (29. 7. 2020).
LOEW, A., LUDWIG, R., MAUSER, W. (2006): Derivation of surface soil moisture from ENVISAT ASAR wide swath and image mode data in agricultural areas. IEEE Transactions on Geoscience and Remote Sensing, 4, 44, 889–898.
LUCKMAN, A. J. (1998): The effects of topography on mechanisms of radar backscatter from coniferous forest and upland pasture. IEEE Transactions on Geoscience and Remote Sensing, 5 PART 2, 36, 1830–1834.
MAKYNEN, M., KARVONEN, J. (2017): Incidence Angle Dependence of First-Year Sea Ice Backscattering Coefficient in Sentinel-1 SAR Imagery over the Kara Sea. IEEE Transactions on Geoscience and Remote Sensing, 11, 55, 6170–6181.
MITCHELL, A. L., ROSENQVIST, A., MORA, B. (2017): Current remote sensing approaches to monitoring forest degradation in support of countries measurement, reporting and verification (MRV) systems for REDD+. Carbon Balance and Management, 1, 12.
MLADENOVA, I. E., JACKSON, T. J., BINDLISH, R., HENSLEY, S. (2013): Incidence angle normalization of radar backscatter data. IEEE Transactions on Geoscience and Remote Sensing, 3, 51, 1791–1804.
MOUGIN, D., LOPES, A., FRISON, P. L., PROISY, C. (1995): Preliminary analysis of ERS-1 wind Scatterometer data over land surfaces. International Journal of Remote Sensing, 2, 16, 391–398.
NGUYEN, D. B., CLAUSS, K., CAO, S., NAEIMI, V., KUENZER, C., WAGNER, W. (2015): Mapping Rice Seasonality in the Mekong Delta with multi-year envisat ASAR WSM Data. Remote Sensing, 12, 7, 15868–15893.
OLESK, A., VOORMANSIK, K., PÕHJALA, M., NOORMA, M. (2015): Forest change detection from Sentinel-1 and ALOS-2 satellite images. Proceedings of the 2015 IEEE 5th Asia-Pacific Conference on Synthetic Aperture Radar, APSAR 2015, 2, 522–527.
PAIRMAN, D., BELLISS, S. E., MCNEILL, S. J. (1997): Terrain Influences on SAR Backscatter around Mt. Taranaki, New Zealand. IEEE Transactions on Geoscience and Remote Sensing, 4, 35, 924–932.
PALOSCIA, S. (1998): An empirical approach to estimating leaf area index from multifrequency SAR data. International Journal of Remote Sensing, 2, 19, 359–364.
PALOSCIA, S., SANTI, E., PETTINATO, S. (2015): Microwave remote sensing for the monitoring of forest ecosystems - presentation.
PATHE, C., WAGNER, W., SABEL, D., DOUBKOVA, M., BASARA, J. B. (2009): Using ENVISAT ASAR global mode data for surface soil moisture retrieval over

Oklahoma, USA. IEEE Transactions on Geoscience and Remote Sensing, 2, 47, 468–480.
PATNAIK, S. C. (2017): Basics of microwave data and analysis for forest study. In: ERTD TREES Training - SAR & Hyperspectral Data Analysis for Forest Applications. 17–26.
PROISY, C., MOUGIN, E., DUFRÊNE, E., DANTEC, V. Le (2000): Monitoring seasonal changes of a mixed temperate forest using ERS SAR observations. IEEE Transactions on Geoscience and Remote Sensing, 1 II, 38, 540–552.
RANSON, K. J., KOVACS, K., SUN, G., KHARUK, V. I. (2003): Disturbance recognition in the boreal forest using radar and Landsat-7. Canadian Journal of Remote Sensing, 2, 29, 271–285.
RANSON, K. J., SUN, G. (2000): Effects of environmental conditions on boreal forest classification and biomass estimates with SAR. IEEE Transactions on Geoscience and Remote Sensing, 3, 38, 1242–1252.
RAUSTE, Y. (1990): Incidence-angle dependence in forested and non-forested areas in Seasat SAR data. International Journal of Remote Sensing, 7, 11, 1267–1276.
RAUSTE, Y., ANTROPOV, O., MUTANEN, T., HÄME, T. (2016): On clear-cut mappingwith time-series of Sentinel-1 data in boreal forest-extended absract. European Space Agency, (Special Publication) ESA SP, May, SP-740, 9–13.
REICHE, J., HAMUNYELA, E., VERBESSELT, J., HOEKMAN, D., HEROLD, M. (2018): Improving near-real time deforestation monitoring in tropical dry forests by combining dense Sentinel-1 time series with Landsat and ALOS-2 PALSAR-2. Remote Sensing of Environment, October 2017, 204, 147–161.
RICHARDS, J. A. (2009): Remote Sensing with Imaging Radar. Springer Berlin Heidelberg, Berlin, Heidelberg.
RIZZOLI, P., BRAUTIGAM, B. (2014): Radar backscatter modeling based on global TanDEM-X mission data. IEEE Transactions on Geoscience and Remote Sensing, 9, 52, 5974–5988.
RÜETSCHI, M., SCHAEPMAN, M. E., SMALL, D. (2018): Using multitemporal Sentinel-1 C-band backscatter to monitor phenology and classify deciduous and coniferous forests in Northern Switzerland. Remote Sensing, 1, 10, 1–30.
RÜETSCHI, M., SMALL, D., WASER, L. T. (2019): Rapid detection of windthrows using Sentinel-1 C-band SAR data. Remote Sensing, 2, 11, 1–23.
SANTILLAN, J. R., MAKINANO-SANTILLAN, M. (2016): Vertical accuracy assessment of 30-M resolution ALOS, ASTER, and SRTM global DEMS over Northeastern Mindanao, Philippines. International Archives of the Photogrammetry, Remote Sensing and Spatial Information Sciences - ISPRS Archives, June, 41, 149–156.
SHARMA, R., LECKIE, D., HILL, D., CROOKS, B., BHOGAL, A. S., ARBOUR, P., D'EON, S. (2005): Hyper-temporal Radarsat SAR data of a forested terrain. Proceedings of the Third International Workshop on the Analysis of Multi-Temporal Remote Sensing Images 2005, C, 2005, 71–75.
SMALL, D. (2011): Flattening gamma: Radiometric terrain correction for SAR imagery. IEEE Transactions on Geoscience and Remote Sensing, 8, 49, 3081–3093.
STYCH, P., JERABKOVA, B., LASTOVICKA, J., RIEDL, M., PALUBA, D. (2019): A Comparison of WorldView-2 and Landsat 8 Images for the Classification of Forests Affected by Bark Beetle Outbreaks Using a Support Vector Machine and a Neural Network: A Case Study in the Sumava Mountains. Geosciences, 9, 9, 396.
ŠTYCH, P., LAŠTOVIČKA, J., HLADKÝ, R., PALUBA, D. (2019): Evaluation of the Influence of Disturbances on Forest Vegetation Using the Time Series of Landsat Data :

A Comparison Study of the Low Tatras and Sumava National Parks. International Journal of Geo-Information, 8, 71, 1–28.
SUN, G., SIMONETT, D. S. (1988): A composite L-band HH radar backscattering model for coniferous forest stands. Photogrammetric Engineering & Remote Sensing, 8, 54, 1195–1201.
SZIGARSKI, C., JAGDHUBER, T., BAUR, M., THIEL, C., PARRENS, M., WIGNERON, J.-P., PILES, M., ENTEKHABI, D. (2018): Analysis of the Radar Vegetation Index and Potential Improvements. Remote Sensing, 11, 10, 1776.
TANASE, M. A., APONTE, C., MERMOZ, S., BOUVET, A., LE TOAN, T., HEURICH, M. (2018): Detection of windthrows and insect outbreaks by L-band SAR: A case study in the Bavarian Forest National Park. Remote Sensing of Environment, April 2017, 209, 700–711.
TANASE, M. A., VILLARD, L., PITAR, D., APOSTOL, B., PETRILA, M., CHIVULESCU, S., LECA, S., BORLAF-MENA, I., PASCU, I. S., DOBRE, A. C., PITAR, D., GUIMAN, G., LORENT, A., ANGHELUS, C., CICEU, A., NEDEA, G., STANCULEANU, R., POPESCU, F., APONTE, C., BADEA, O. (2019): Synthetic aperture radar sensitivity to forest changes: A simulations-based study for the Romanian forests. Science of the Total Environment, 689, 1104–1114.
TEILLET, P. M., GUINDON, B., MEUNIER, J. F., GOODENOUGH, D. G. (1985): Slope-aspect effects in synthetic aperture radar imagery. Canadian Journal of Remote Sensing, 1, 11, 39–49.
TOPOUZELIS, K., SINGHA, S. (2016): Incidence angle Normalization of Wide Swath SAR Data for Oceanographic Applications. Open Geosciences, 1, 8, 450–464.
TORRES, R., BUCK, C., GUIJARRO, C., SUCHAIL, J.-L., SCHÖNENBERG, A. (2000): The Envisat ASAR Instrument Verification and Characterisation. Proceedings of the 1999 SAR Workshop: CEOS Committee on Earth Observation Satellites; Working Group on Calibration, April, 303–310.
TORRES, R., SNOEIJ, P., GEUDTNER, D., BIBBY, D., DAVIDSON, M., ATTEMA, E., POTIN, P., ROMMEN, B. Ö., FLOURY, N., BROWN, M., TRAVER, I. N., DEGHAYE, P., DUESMANN, B., ROSICH, B., MIRANDA, N., BRUNO, C., L'ABBATE, M., CROCI, R., PIETROPAOLO, A., HUCHLER, M., ROSTAN, F. (2012): GMES Sentinel-1 mission. Remote Sensing of Environment, 120, 9–24.
TRUCKENBRODT, J., FREEMANTLE, T., WILLIAMS, C., JONES, T., SMALL, D., DUBOIS, C., THIEL, C., ROSSI, C., SYRIOU, A., GIULIANI, G. (2019): Towards sentinel-1 SAR analysis-ready data: A best practices assessment on preparing backscatter data for the cube. Data, 3, 4.
ULABY, F. T., MOORE, R. K., FUNG, A. K. (1981): Microwave Remote Sensing: Active and Passive, Volume I: Fundamentals and Radiometry. Artech House Publishers.
ULANDER, L. M. H. (1996): Radiometrie slope correction of synthetic-aperture radar images. IEEE Transactions on Geoscience and Remote Sensing, 5, 34, 1115–1122.
VAN ZYL, J. J. (1993): The effect of topography on radar scattering from vegetated areas. IEEE TRANSACTIONS ON GEOSCIENCE AND REMOTE SENSING, 1, 2, 1132–1134.
VAN ZYL, J. J., CHAPMAN, B. D., DUBOIS, P., SHI, J. (1993): The Effect of Topography on SAR Calibration. IEEE Transactions on Geoscience and Remote Sensing, 5, 31, 1036–1043.
WAGNER, W., NOLL, J., BORGEAUD, M., ROTT, H. (1999): Monitoring soil moisture over the canadian prairies with the ERS scatterometer. IEEE Transactions on Geoscience and Remote Sensing, 1 PART 1, 37, 206–216.
WALKER, W. (2016): Introduction to RADAR Remote Sensing for Vegetation

Mapping and Monitoring.
WIDHALM, B., BARTSCH, A., GOLER, R. (2018): Simplified normalization of C-band synthetic aperture radar data for terrestrial applications in high latitude environments. Remote Sensing, 4, 10, 1–18.
WU, S. T. (1985): Preliminary Report on the Measurements of Forest Canopies With C-Band Radar Scatterometer At Nasa/Nstl. Digest - International Geoscience and Remote Sensing Symposium (IGARSS), 6, 168–173.
YUNJIN KIM, VAN ZYL, J. (2002): Comparison of forest parameter estimation techniques using SAR data. In: IGARSS 2001. Scanning the Present and Resolving the Future. Proceedings. IEEE 2001 International Geoscience and Remote Sensing Symposium (Cat. No.01CH37217). IEEE, 1395–1397.
ZHOU, C., ZHENG, L. (2017): Mapping radar glacier zones and dry snow line in the antarctic peninsula using Sentinel-1 images. Remote Sensing, 11, 9, 1–19.

Appendices

Appendix 1 Distribution of generated forest areas according to LIA for study area 1

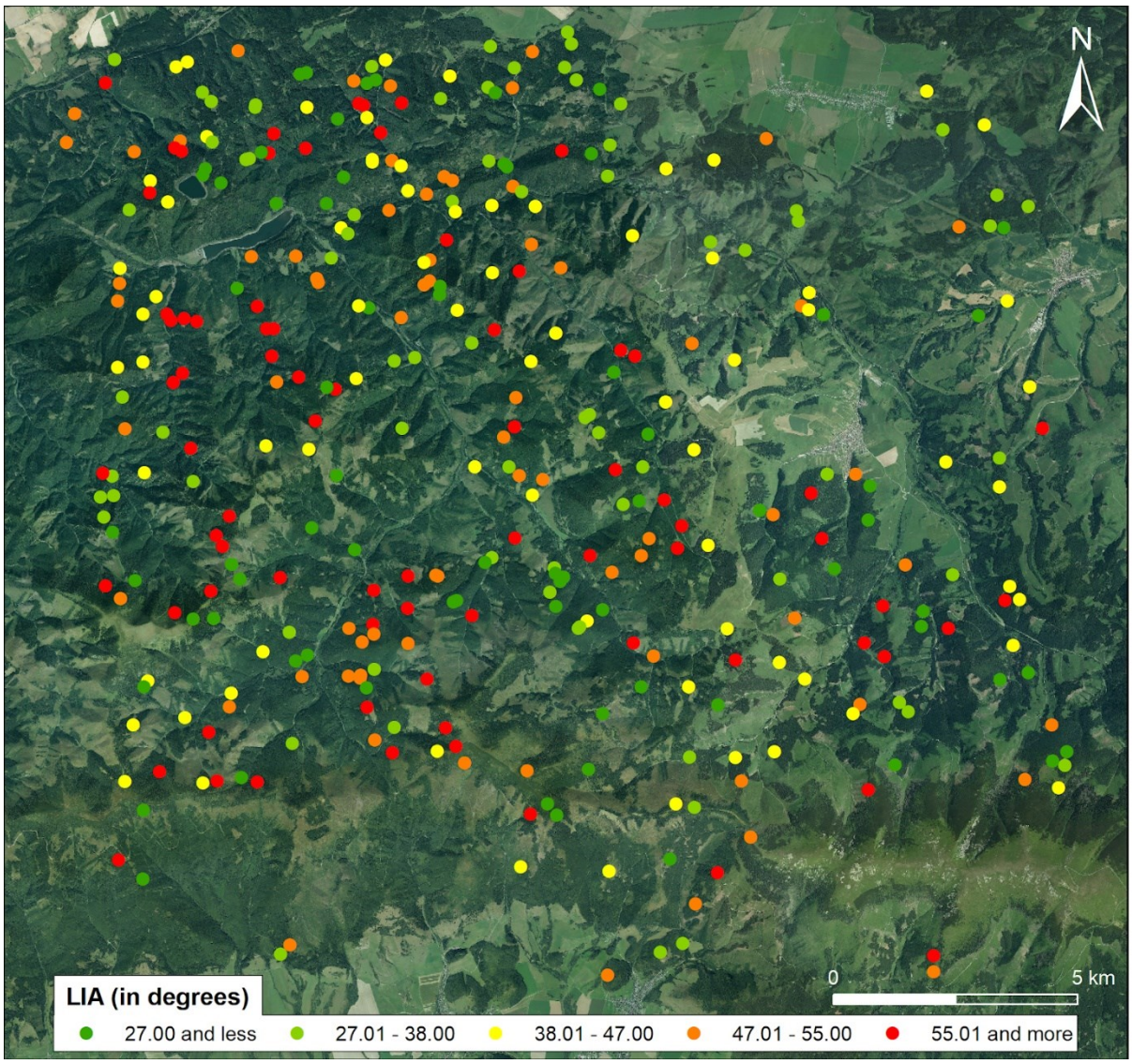

Source: own work. Base map source: Web Map Service ZBGIS (Digital map app) by Geodesy, Cartography and Cadastre Authority of the Slovak Republic (UGKK SR) (2018).

Explanatory notes: Size of forest areas do not correspond to the real area used for analysis. They are enlarged for better visualisation purposes.

Appendix 2 Description of GEE JavaScript codes

The digital appendix of the thesis includes five different JavaScript codes for GEE:

- The code "LIA_Correction_Function_for_GEE.js" includes a freely available algorithm to correct the backscatter-LIA dependence in a SAR image collection, available also in GEE at https://code.earthengine.google.com/d1e71db16a0a8861269469b0b914a2d8. The usage and documentation for the algorithm are described in the Appendix 3 and Appendix 4, respectively.
    - Code "LIA_Correction_Example.js" represents an example usage of this algorithm on all available Sentinel-1 data for a three month-long period over a selected area in Low Tatras National Park – the user will get a Time Series for corrected and uncorrected backscatter values for both polarization.
    - Code named “CaseStudiesStats.js” contains JavaScript code for calculation of characteristics of four case studies, while “StudyAreasStats.js” contains code for calculation of characteristics of selected 15 study areas.
    - Code “Other_statistics_and_Graphs.js” contains code for generation of statistical parameters and graphs for a given study area.
    - Text file “Usage and documentation for the algorithm.txt” contains description how to use this algorithm in GEE and documentation for the algorithm parameters.

Appendix 3 Description of usage of the proposed LIACorrection algorithm in GEE

This algorithm can be used after the requirement call "require('users/danielp/LIA_Correction:LIA_Correction_Function')" (see code "LIA_Correction_Example.js") or by copying the code in the "LIA_Correction_Function_for_GEE.js" file to the GEE Code Editor and call it with defined parameters.

Appendix 4 Documentation for the LIACorrection algorithm parameters

Parameter	Type	Description
ROI	Geometry	Define the ROI for what you want to create a Time Series Analysis
startDate	Date	Start date of the Time Series
endDate	Date	End date of the Time Series
landCoverType	Integer	Define the land cover type. Currently supported for coniferous forest (312) and broadleaf forest (311).
boudningBoxSize	Integer (optional, default: 10000)	The bounding box size around the selected area to calculate the backscatter-LIA dependence.
referenceAngle	Integer (optional, deafault: 9999)	Reference angle to which the backscatter values will be corrected. The default value 9999 represents the mean value from the minimum and maximum value of observed LIA (from the available paths).
SARCollection	ImageCollection (optional, default: Sentinel-1 ImageCollection with VV and VH bands)	Select the SAR image collection for which you want to apply the LIA correction. Tested for Sentinel-1 data.
acquistionMode	String (optional, default: 'IW')	Acqusition mode for Sentinel-1 data in GEE can be 'IW' (Interferometric Wide Swath), 'EW' (Extra Wide Swath) or 'SM' (Strip Map).